

The curious case of EP241021a: Unraveling the mystery of its exceptional rebrightening

Malte Busmann^{1,*}, Brendan O’Connor^{2,**}, Julian Sommer¹, Daniel Gruen^{1,3}, Paz Beniamini^{4,5,6}, Ramandeep Gill^{7,5}, Michael J. Moss⁸, Antonella Palmese², Arno Riffeser^{1,10}, Yu-Han Yang¹¹, Eleonora Troja¹¹, Simone Dichiaro¹², Roberto Ricci^{11,13}, Noel Klingler^{8,14,15}, Claus Gössl¹, Lei Hu², Arne Rau¹⁰, Christoph Ries¹, Geoffrey Ryan¹⁶, Michael Schmidt¹, Muskan Yadav¹¹, and Gregory R. Zeimann¹⁷

- ¹ University Observatory, Faculty of Physics, Ludwig-Maximilians-Universität München, Scheinerstr. 1, 81679 Munich, Germany
e-mail: m.busmann@physik.lmu.de
- ² McWilliams Center for Cosmology and Astrophysics, Department of Physics, Carnegie Mellon University, Pittsburgh, PA 15213, USA
e-mail: boconno2@andrew.cmu.edu
- ³ Excellence Cluster ORIGINS, Boltzmannstr. 2, 85748 Garching, Germany
- ⁴ Department of Natural Sciences, The Open University of Israel, P.O Box 808, Ra’anana 43537, Israel
- ⁵ Astrophysics Research Center of the Open university (ARCO), The Open University of Israel, P.O Box 808, Ra’anana 43537, Israel
- ⁶ Department of Physics, The George Washington University, Washington, DC 20052, USA
- ⁷ Instituto de Radioastronomía y Astrofísica, Universidad Nacional Autónoma de México, Antigua Carretera a Pátzcuaro # 8701, Ex-Hda. San José de la Huerta, Morelia, Michoacán, C.P. 58089, México
- ⁸ Astrophysics Science Division, NASA Goddard Space Flight Center, Mail Code 661, Greenbelt, MD 20771, USA
- ⁹ NASA Postdoctoral Program Fellow, NASA Goddard Space Flight Center, Greenbelt, MD 20771, USA
- ¹⁰ Max-Planck-Institut für Extraterrestrische Physik, Giessenbachstraße 1, 85748 Garching, Germany
- ¹¹ Department of Physics, University of Rome “Tor Vergata”, via della Ricerca Scientifica 1, I-00133 Rome, Italy
- ¹² Department of Astronomy and Astrophysics, The Pennsylvania State University, 525 Davey Lab, University Park, PA 16802, USA
- ¹³ INAF-Istituto di Radioastronomia, Via Gobetti 101, I-40129 Bologna, Italy
- ¹⁴ Center for Space Sciences and Technology, University of Maryland, Baltimore County, Baltimore, MD 21250, USA
- ¹⁵ Center for Research and Exploration in Space Science and Technology, NASA/GSFC, Greenbelt, Maryland 20771, USA
- ¹⁶ Perimeter Institute for Theoretical Physics, Waterloo, Ontario N2L 2Y5, Canada
- ¹⁷ University of Texas, Hobby–Eberly Telescope, McDonald Observatory, TX 79734, USA

March 20, 2025

ABSTRACT

Context. Fast X-ray Transients (FXTs) are a rare and poorly understood phenomenon with a variety of possible progenitors. The launch of the *Einstein Probe* (EP) mission has facilitated a rapid increase in the real-time discovery and follow-up of FXTs.

Aims. We focus on the recent EP discovered transient EP241021a, which shows a peculiar panchromatic behavior, with the aim to understand its origin.

Methods. We obtained optical and near-infrared multi-band imaging and spectroscopy with the Fraunhofer Telescope at Wendelstein Observatory, the Hobby–Eberly Telescope, and the Very Large Telescope, of the new EP discovered transient EP241021a over the first 100 days of its evolution.

Results. EP241021a was discovered by EP as a soft X-ray trigger, but was not detected at gamma-ray frequencies. The observed soft X-ray prompt emission spectrum is consistent with non-thermal radiation, which requires at least a mildly relativistic outflow with bulk Lorentz factor $\Gamma \gtrsim 4$. The optical and near-infrared lightcurve displays a two component behavior where an initially fading component $\sim t^{-1}$ turns to a rise steeper than $\sim t^4$ after a few days before peaking at an absolute magnitude $M_r \approx -22$ mag and quickly returning to the initial decay. The peak absolute magnitude is the most luminous optical emission associated to an FXT, superseding EP240414a. Standard supernova models are unable to reproduce either the absolute magnitude or rapid timescale (< 2 d) of the rebrightening. The X-ray, optical and near-infrared spectral energy distributions display a red color $r - J \approx 1$ mag, and point to a non-thermal origin ($\sim \nu^{-1}$) for the broadband emission. By considering a gamma-ray burst as a plausible scenario, we favor a refreshed shock as the cause of the rebrightening. This is consistent with the inference of an at least mildly relativistic outflow based on the prompt trigger.

Conclusions. Our results suggest a likely link between EP discovered FXTs and low luminosity gamma-ray bursts.

Key words. X-rays: general – X-rays: bursts – Gamma-ray burst: general – Stars: jets

1. Introduction

The *Einstein probe* (EP) is a new soft X-ray mission (Yuan et al. 2015, 2022, 2025) with wide-field capabilities. The Wide-field X-ray Telescope (WXT) has an instantaneous field-of-view

* Recipient of a Wübben Stiftung Wissenschaft Student Grant

** McWilliams Fellow

(FOV) of 3,600 deg² observing in the soft X-ray band between 0.4 – 4.0 keV. This revolutionary wide-field X-ray survey capability, and on-board triggering, is able to unlock the previously hidden transient X-ray sky, acting in a similar fashion for X-ray transients as gamma-ray monitors such as the *Neil Gehrels Swift Observatory* (Gehrels et al. 2004) and *Fermi Gamma-ray Space Telescope* (Meegan et al. 2009) do for gamma-ray bursts (GRBs).

In the first year since its launch, EP has rapidly identified a number of rare X-ray transients, allowing for key follow-up at other wavelengths. Many of these on-board triggers are found to be extragalactic transients, such as GRBs. These include EP240219a (Yin et al. 2024), EP240315a/GRB 240315C (Levan et al. 2024; Liu et al. 2024; Gillanders et al. 2024; Ricci et al. 2024b) and EP240414a (Srivastav et al. 2024; van Dalen et al. 2024; Bright et al. 2024; Sun et al. 2024), EP240801a (Jiang et al. 2025), among others (e.g., Yin et al. 2024; Liu et al. 2024). The interpretation of some other EP transients has been less clear, and some may represent a new class of high-energy transients (e.g., EP240408a; O’Connor et al. 2025; Zhang et al. 2025). Comprehensive multi-wavelength follow-up is urgently required for revealing the nature and astrophysical diversity of these events.

Of particular interest regarding EP240414a ($z=0.4$) are its multiple optical emission components (Srivastav et al. 2024; van Dalen et al. 2024; Sun et al. 2024), including clear evidence for a supernova (SN), see van Dalen et al. (2024). The fast timescale of the optical transient can be linked to Fast Blue Optical Transients (FBOTs; Drout et al. 2014; Pursiainen et al. 2018; Prentice et al. 2018; Margutti et al. 2019; Perley et al. 2019; Ho et al. 2023a) while the lack of a gamma-ray trigger and low peak energy (Sun et al. 2024) match characteristics of low luminosity GRBs (Galama et al. 1998; Malesani et al. 2004; Sakamoto et al. 2004; Soderberg et al. 2004a,b, 2006; Starling et al. 2011; Izzo et al. 2019; H. E. S. S. Collaboration et al. 2021). Therefore, EP240414a appears to potentially be the missing link between multiple classes of high-energy sources, though the connection is still inconclusive (Srivastav et al. 2024). This is challenging to solidify as the production of low luminosity GRBs is still not well understood (see, e.g., Irwin & Hotokezaka 2024c,b,a). An alternative interpretation is that EP240414a represents an entirely different class of transient that had not been previously observed.

In this manuscript, we present our multi-wavelength campaign of the recently discovered EP241021a. We find that EP241021a presents a similar behavior to EP240414a in its multiple, clearly distinct emission episodes. Localized to redshift $z=0.75$ (Pugliese et al. 2024; Pérez-Fournon et al. 2024; Zheng et al. 2024a), EP241021a has a peak absolute magnitude of $M_r \approx -22$ mag, making this the most luminous optical emission from a fast X-ray transient, and a timescale of only a few days after the peak. We analyze the X-ray, optical, near-infrared and radio dataset of EP241021a to determine whether it requires multiple emission components or can potentially be explained by the same outflow. We further connect EP241021a to the previous peculiar EP transient EP240414a and discuss the possible interpretations for their multiwavelength behavior.

Throughout the manuscript we adopt a standard Λ CDM-cosmology (Planck Collaboration et al. 2020). We also adopt the convention for the flux density $F_\nu \propto t^\alpha \nu^\beta$ where α is the temporal index and β is the spectral index. All upper limits are reported at the 3σ level and all magnitudes are in the AB system.

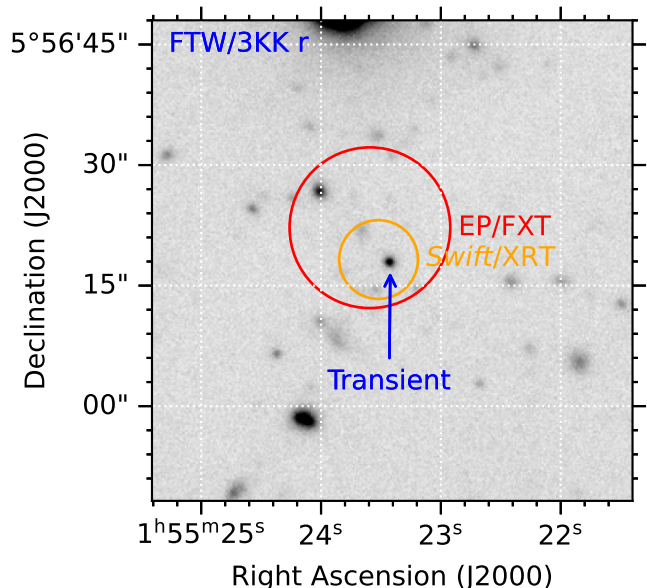


Fig. 1: Finding chart of EP241021a combining all FTW exposures in r -band (38.1 hr total). The location of the transient (blue) lies within the X-ray localizations from *Swift*/XRT (orange) and EP/FXT (red).

2. Observations

2.1. Prompt X-ray Trigger and Gamma-ray Limits

The Wide-field X-ray Telescope (WXT) onboard the *Einstein Probe* (EP; Yuan et al. 2015, 2022, 2025) triggered on EP241021a on 2024-10-21 at 05:07:56 UT (Hu et al. 2024). The source had a duration of ~ 100 s with a time-averaged X-ray flux (0.5 – 4.0 keV) of $3.3_{-1.6}^{+4.8} \times 10^{-10}$ erg cm⁻² s⁻¹ (90% confidence level; CL). The soft X-ray fluence is approximately $\sim 3.3 \times 10^{-9}$ erg cm⁻², yielding an estimate of the isotropic-equivalent energy (0.5 – 4.0 keV) of $(5.1_{-2.5}^{+7.5}) \times 10^{49}$ erg at $z=0.75$ (Pugliese et al. 2024; Pérez-Fournon et al. 2024; Zheng et al. 2024a).

At the time of the EP trigger *Konus-Wind* was observing the entire sky, but did not detect EP241021a in gamma-rays (Svinkin et al. 2024). The 90% confidence upper limit to the peak gamma-ray flux (20 – 1,500 keV) is $< 2.5 \times 10^{-7}$ erg cm⁻² s⁻¹ assuming a timescale of 2.944 s (Svinkin et al. 2024). We adopt a typical long GRB spectrum characterized by a Band function (Band et al. 1993) with peak energy $E_p = 70 - 300$ keV and low and high spectral indices $\alpha = -1$ and $\beta = -2.5$, respectively. This is roughly consistent with the photon index determined from the initial EP trigger, $\Gamma = -1.5 \pm 1.2$ at the 90% CL (Hu et al. 2024). This bolometric correction yields an upper limit to the isotropic-equivalent gamma-ray energy of $\lesssim 10^{51}$ erg for the gamma-ray fluence in the 1 – 10,000 keV energy range. We discuss these implications further in §4.5.

2.2. Fraunhofer Telescope Wendelstein (FTW)

We observed the optical and near-infrared (OIR) counterpart of EP241021a with the Three Channel Imager (3KK; Lang-Bardl et al. 2016) on the 2.1 m Fraunhofer Telescope at Wendelstein Observatory (FTW; Hopp et al. 2014) located on Mt. Wendelstein at the northern edge of the Alps. 3KK can observe a $7' \times 7'$ FOV in three channels simultaneously. The blue channel can ob-

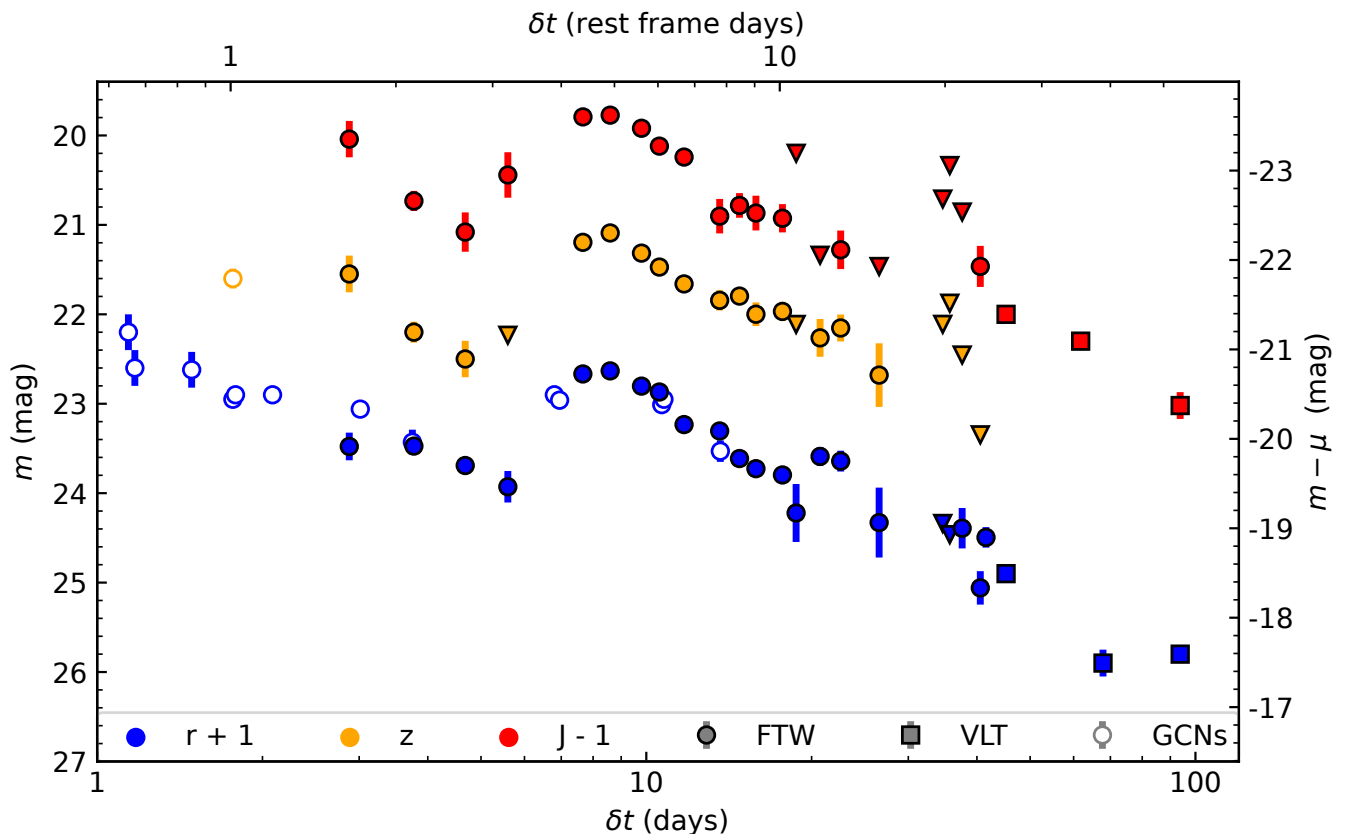


Fig. 2: Optical to near-infrared lightcurve of EP241021a in the r , i , J filters. We present our observations obtained with the FTW and the VLT, and supplement these data with observations reported in GCN Circulars (Fu et al. 2024b,a; Li et al. 2024c; Ror et al. 2024; Li et al. 2024b; Zheng et al. 2024b; Pugliese et al. 2024; Bochenek & Perley 2024a; Quirola-Vasquez et al. 2024; Freeburn et al. 2024a; Schneider & Adami 2024b; Bochenek & Perley 2024b; Schneider & Adami 2024a). The apparent magnitude m and absolute magnitude M , and observer frame and rest frame time are shown on the four sides assuming $z=0.75$.

serve either in the u' , g' or r' band, the red channel in the i' or z' band, and the NIR channel supports the Y , J , H and K_s bands. Data were obtained 22 times between 2024-10-23T02:12:17 UT (2.8 d after the EP-WXT trigger) and 2024-12-01T18:26:38 UT (43 d after the EP-WXT trigger) in the r' , i' , z' , J , and H band. The majority of observations were obtained simultaneously in the $r'z'J$ filters.

The data were reduced and analyzed using a custom data analysis pipeline based on Gössl & Riffeser (2002) that applies standard image processing techniques such as bias and dark subtraction, flat-fielding, cosmic ray rejection, among other corrections. The images were stacked using tools from the AstrOmatic software suite (Bertin & Arnouts 1996; Bertin et al. 2002; Bertin 2006). The OIR counterpart is detected throughout our observations (see Figure 1), which include a net 38.1 hr of exposure with the 3KK imager. Archival observations as part of the DESI Legacy Surveys do not reveal an underlying galaxy to deep limits (Fu et al. 2024b), and as such we do not perform difference imaging due to the lack of existing templates or a known host galaxy brightness. Aperture photometry of the OIR counterpart was computed using Photutils (Bradley et al. 2024) and calibrated to the 2MASS (Skrutskie et al. 2006) and PS1 (Chambers et al. 2016) catalogs. The photometry is tabulated in Table A.1 and displayed in Figure 2.

2.3. Hobby-Eberly Telescope (HET)

We observed EP241021a with the 11 m Hobby-Eberly Telescope (HET; Ramsey et al. 1998; Hill et al. 2021) at McDonald Observatory through program M24-3-005 (PI: Gruen) on 2024-10-25, 2024-10-29, and 2024-11-26 (see Table A.2). The observations were scheduled using the HET's queue scheduling system (Shetrone et al. 2007). We used the low-resolution integral-field spectrograph (LRS2; Chonis et al. 2014, 2016) to obtain spectra in both wavelength channels with LRS2-B (370-700 nm) and LRS2-R (650-1050 nm). LRS2-B data were obtained on 2024-10-25 and LRS2-R on both 2024-10-29 and 2024-11-26 (Table A.2). The raw LRS2 data are initially processed with Panacea¹, which carries out bias subtraction, dark subtraction, fiber tracing, fiber wavelength evaluation, fiber extraction, fiber-to-fiber normalization, source detection, source extraction, and flux calibration for each channel. The absolute flux calibration comes from default response curves and measures of the mirror illumination as well as the exposure throughput from guider images. We extracted the flux-calibrated one-dimensional spectrum with the LRS2Multi² package to integrate over the 0.59'' fibers in a 1.0–1.5'' aperture centered on EP241021a. The signal-to-noise (SNR) ratio in these observations is quite low and we are

¹ <https://github.com/grzeimann/Panacea>

² <https://github.com/grzeimann/LRS2Multi>

only able to confirm the [OII] emission line at 6519 Å corresponding to $z = 0.75$, as previously reported as the redshift of underlying emission lines and absorption lines in the transient spectra (Pugliese et al. 2024; Pérez-Fournon et al. 2024; Zheng et al. 2024a). These features provide a secure redshift for EP241021a. We do not identify any supernova-like features in these HET spectra, though, as noted, the SNR of the continuum emission is quite low.

2.4. Very Large Telescope (VLT)

We carried out multi-band observations of EP241021a with the Very Large Telescope (VLT) at Cerro Paranal, Chile using the FORS2 (Appenzeller et al. 1998) and HAWK-I (Kissler-Patig et al. 2008) instruments under program 114.27LW (PI: Troja). Data were obtained on 2024-12-05 and 2024-12-28 in *R*-band (1200 s) with FORS2, and 2024-12-05 and 2024-12-22 in *J*-band (900 s) with HAWK-I. Additional data was obtained on 2025-01-23 in both filters with exposures of 1200 s. The data were reduced using the standard ESO Data Reduction Pipelines and the individual images were combined using SWarp (Bertin 2010) to create a stacked image. Photometry was performed with SExtractor (Bertin & Arnouts 1996) and calibrated to the 2MASS (Skrutskie et al. 2006) and PS1 (Chambers et al. 2016) catalogs.

2.5. Neil Gehrels Swift Observatory

The position of EP241021a was observed by the *Neil Gehrels Swift Observatory* (hereafter *Swift*; Gehrels et al. 2004) X-ray Telescope (XRT; Burrows et al. 2005a) between 2024-10-24 and 2024-11-15 (ObsIDs: 21725 and 1889) for seven visits totaling 17.5 ks in Photon Counting (PC) mode. We used the *Swift*/XRT data products generator³ to analyze these data. An X-ray source is detected on 2024-10-29, 2024-11-07, and 2024-11-15 and localized to RA, DEC (J2000) = $01^h55^m23^s.53$, $+05^{\circ}56'18.3''$ with uncertainty of $4.9''$ (90% CL). This position is consistent with the optical localization of the transient.

The X-ray source is weak and the spectrum is not well-constrained. A fit to the time-averaged X-ray spectrum with an absorbed powerlaw model yields a photon index of $\Gamma \approx -2.0^{+1.8}_{-0.6}$ and an unabsorbed energy conversion factor of $\approx 3.3 \times 10^{-11}$ erg cm^{-2} cts^{-1} with the hydrogen column density fixed to the line-of-sight Galactic value ($N_H = 5 \times 10^{20}$ cm^{-2} , Willingale et al. 2013). The log of X-ray observations is reported in Table A.3.

The *Swift* Ultra-Violet Optical Telescope (UVOT; Roming et al. 2005) observed EP241021a simultaneously to XRT. The source is detected only in a single epoch on 2024-10-29, as previously reported by Klingler et al. (2024). We extracted upper limits at the source position in all other epochs using the uvotsource task within the HEASoft software. The results are presented in Table A.1.

3. Analysis and Results

3.1. Temporal Evolution

The optical and near-infrared lightcurve of EP241021a displays two clear emission episodes (Figure 2). Around a day after the EP trigger the optical emission was found to be rapidly fading (e.g., Fu et al. 2024b,a; Li et al. 2024c; Ror et al. 2024; Li et al. 2024b), but at ~ 7 d (observer frame; e.g., Quirola-Vasquez

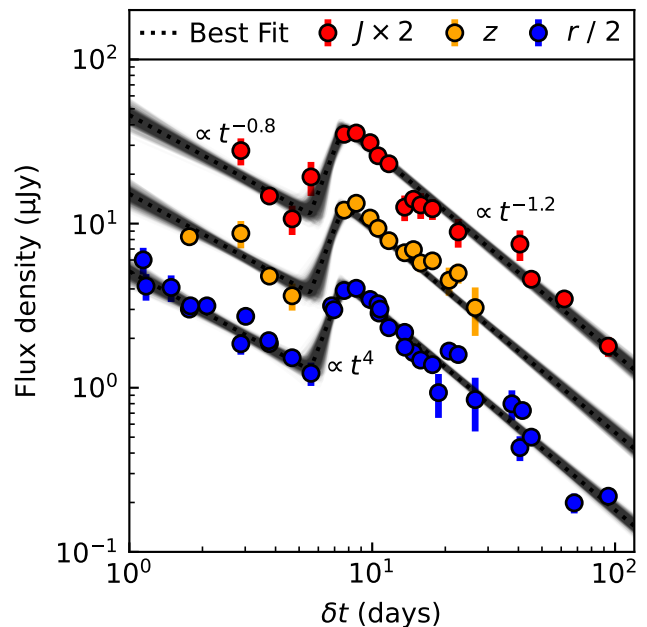


Fig. 3: Temporal powerlaw fit to the OIR lightcurves of EP241021a in the *riJ* filters. The lightcurve clearly displays a rebrightening after ~ 6 d.

et al. 2024; Freeburn et al. 2024a) the transient was observed to have rapidly brightened by ~ 1 mag, peaking by ~ 8 d (observer frame). After the peak, the transient again returned to a steep decay. Our observations with FTW began at 2.9 d (observer frame), see Table A.1. We supplemented our dataset with early time photometry reported in GCN Circulars⁴, as shown in Figure 2.

As described above, the lightcurve behavior can be clearly separated into two components (Figure 2), which we refer to as the first and second component, respectively. We roughly separate these by defining the first component as the early fading behavior at < 6 d (observer frame), and the second component as all other OIR data obtained between $\sim 6 - 100$ d. To constrain the temporal behavior, we model the OIR lightcurve, including both components, with a double smoothly broken powerlaw t^α with temporal slope α . Parameter estimation was performed using the emcee (Foreman-Mackey et al. 2013) and ChainConsumer (Hinton 2016) packages. The results of our temporal fit to the lightcurves are shown in Figure 3. The initial segment shows a decay of $\alpha_1 = -0.81^{+0.08}_{-0.07}$, followed by a steep rise of $\alpha_2 = 3.6^{+3.0}_{-0.9}$. The exact rising phase is not well constrained by the data, but the 90% confidence lower limit to the rising slope is found to be $\alpha_2 \gtrsim 3.2$. The rise starts at $5.6^{+0.5}_{-0.2}$ d and then peaks at $7.4^{+0.4}_{-0.3}$ d followed again by another decline of $\alpha_3 = -1.24 \pm 0.03$. For the full corner plot, see Figure B.1.

If instead we require that the initial decaying slope α_1 and final decaying slope α_3 are fixed to the same value, we find $\alpha_1 = \alpha_3 = -1.15 \pm 0.04$. This provides a similarly good description of the multi-band OIR data. The reduced chi-squared values for both fits are $\chi^2/\text{dof} \approx 2$.

The *R*-band photometry obtained with the VLT at 68 and 94 d (§2.4) after the EP trigger appear consistent with a flat evolution. While the measurement obtained at 68 d is a marginal deviation from the model ($\sim 2\sigma$), we also consider the possibility

³ https://www.swift.ac.uk/user_objects/

⁴ <https://gcn.nasa.gov/>

that this represents a significant contribution from the underlying host galaxy flux. We therefore also performed the same temporal fit outlined above after artificially subtracting this flux level from the lightcurve, and excluding the last two points from the fit. This does not change either α_1 or α_2 , but does lead to a steeper decaying slope of the second segment with $\alpha_3 = -1.48^{+0.06}_{-0.07}$.

We note that a longer baseline is required to conclusively determine whether this is indeed the host galaxy contribution. In particular, the R -band measurement at 68 d was obtained under poor seeing (full width at half maximum of $\sim 1.7''$), whereas all other data had better image quality with seeing of $0.5 - 0.9''$. Therefore the marginal deviation of the 68 d photometry may be due to the poor conditions.

We likewise model the combined EP/FXT and *Swift*/XRT X-ray lightcurve with a single powerlaw, which yields a temporal index $\alpha_X = -0.5^{+0.4}_{-0.2}$. While this is not as well constrained, it differs significantly from the decay observed at OIR wavelengths, and, despite the large errors on the X-ray data, may imply they arise from separate emission components, as we explore later on. We cannot, however, completely exclude that the X-ray behavior has the same rebrightening as observed at optical wavelengths, which could appear as a flat lightcurve due to poor temporal coverage and low signal-to-noise.

3.2. Spectral Evolution

EP241021a displays a consistent, red color $r - J \approx 1$ mag throughout its entire evolution (see Figure 2). There is marginal evidence for deviation from this value, but the large photometric errors at these phases do not allow for any possible evolution to be confirmed. The red color of the transient is similar to EP240414a, which had $r - z \approx 0.4 \pm 0.1$ mag (Srivastav et al. 2024; van Dalen et al. 2024; Sun et al. 2024). These values are also found for the non-thermal afterglow emission from GRBs.

This motivates us to model the near-simultaneous broadband (X-ray to near-infrared) spectral energy distribution (SED) across multiple epochs using an absorbed powerlaw ν^β with spectral index β . We correct the photometry for Galactic extinction $E(B - V) = 0.045$ mag (Schlafly & Finkbeiner 2011) and further shifted the OIR data to the mid-time of the X-ray observations (Table A.3) using the best-fit temporal index (§3.1).

In Figure 4, we show the XOIR SEDs at observer frame times of $\sim 3, 8, 17,$ and 25 d (observer frame) after the EP trigger. We find $\beta_{XOIR} \approx -1$ (solid lines in Figure 4) is roughly consistent with the data lying on the same spectral powerlaw segment. This interpretation is complicated by *i*) the sparse X-ray data with large error bars on the flux measurements and lack of a well-constrained photon index ($\Gamma = \beta - 1 \approx -2.0^{+1.8}_{-0.6}$) and *ii*) the lack of a similar temporal evolution in the X-ray and OIR bands.

Instead, by modeling the optical data alone we find a spectral index of $\beta_{OIR} = -1.16^{+0.06}_{-0.05}$ (dashed lines in Figure 4). This provides a consistent description of the optical color throughout the evolution of the second component (peak and post-peak of the lightcurve; Figure 2), whereas our data do not provide strong constraints on the pre-peak spectral index. This spectral index is steeper than shown by the solid lines in Figure 4, but does not significantly underpredict the X-ray data by more than 2σ . Therefore the deviation is not well constrained, and while we can conclude the X-ray and optical data are marginally consistent with arising from the same emission component, the sparse data precludes a robust inference.

In either case, the spectral slope very significantly overpredicts the near-simultaneous radio observations (e.g., Yadav et al., in preparation; Schroeder et al. 2024; Ricci et al. 2024a),

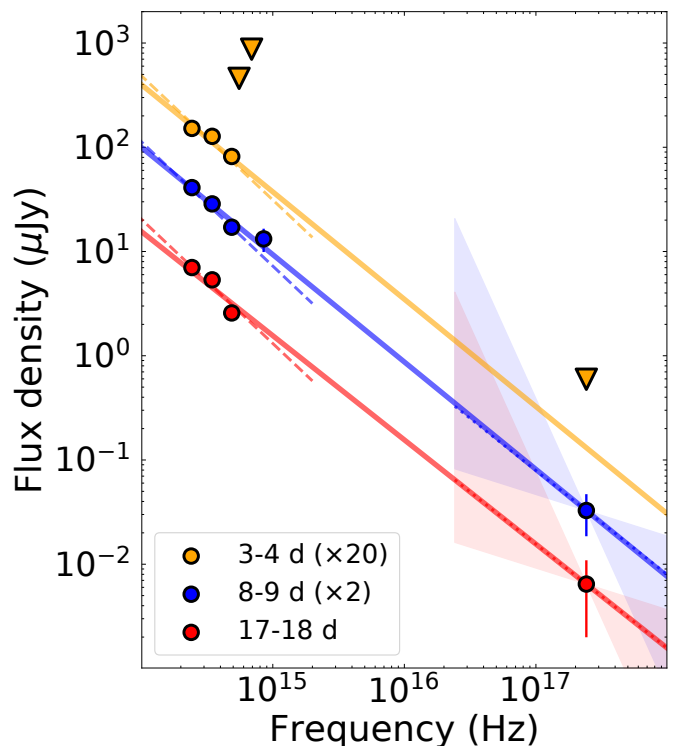


Fig. 4: Multi-epoch spectral energy distribution (SED) of EP241021a from X-ray to near-infrared frequencies using *Swift*/XRT and FTW. The three epochs represent pre-peak, peak, and post-peak SEDs. The uncertainty on the X-ray spectral index ν^β is shown as a shaded region with the median represented by a dotted line. The solid lines connecting the XOIR data assume $\beta_{XOIR} = -1$, whereas the dotted line through the OIR data is the best fit $\beta_{OIR} = -1.16$.

which either signifies a spectral break, or multiple emission mechanisms. The radio data strongly imply the presence of non-thermal radiation (Yadav et al., in preparation).

4. Discussion

4.1. The multi-wavelength properties of EP241021a

Here we briefly summarize the results of our analysis in terms of the multi-wavelength properties of EP241021a:

- The prompt emission at soft X-ray wavelengths is roughly consistent with the energetics of low luminosity GRBs, while it lacked any gamma-ray detection (see §2.1 and Figure 6).
- The OIR lightcurve rebrightens starting sometime after ~ 3.2 d (rest frame) and peaks at ~ 4.5 d (rest frame), see §3.1 and Figure 2.
- The source has a consistently red color ($r - J \approx 1$ mag; §3.2) that is indicative of non-thermal emission (Figure 4).
- The presence of luminous X-ray and radio emission strengthens the evidence for a significant non-thermal component.

These properties make EP241021a rather unique among both high-energy transients and fast optical transients. The main take-aways from this multi-wavelength behavior is that any scenario to explain EP241021a requires either multiple emission components, potentially due to multiple outflows, or a mechanism to produce a rebrightening phase (e.g., energy injection, long-lived

central engine activity, refreshed shock, reverse shock; see §4.7 for further discussion). In the next section, we explore the possible relation to EP240414a, which has shown a roughly similar multi-wavelength behavior.

4.2. A new class of transients: Comparison to EP240414a

Here we summarize the properties of EP240414a, a twin to EP241021a, based on the analyses reported in the literature (Srivastav et al. 2024; van Dalen et al. 2024; Bright et al. 2024; Sun et al. 2024):

- The initial EP trigger is consistent with the energetics of low luminosity GRBs (Figure 6), and the peak energy E_p is strongly constrained to the soft X-ray band (Sun et al. 2024).
- A redshift of $z = 0.401$ was adopted based on the association to a massive host galaxy at a large projected physical offset of ~ 26 kpc (van Dalen et al. 2024; Srivastav et al. 2024).
- The OIR emission was initially slowly fading before re-brightening to $M_r \approx -21$ mag after 2 d (rest frame). This fast timescale is consistent with known FBOTs, but the consistently red color ($r - z = 0.4 \pm 0.1$ mag) clearly separates EP240414a from that class of events (e.g., Drout et al. 2014; Perley et al. 2019; Ho et al. 2019; Margutti et al. 2019; Ho et al. 2020; Coppejans et al. 2020; Perley et al. 2021).
- A third component ($M_r \approx -19.5$ mag) appeared after ~ 15 d (rest frame), which was spectroscopically confirmed as a Type Ic-BLe supernova (van Dalen et al. 2024), consistent with the canonical GRB-SN (e.g., Cano et al. 2017) SN 1998bw (e.g., Galama et al. 1998). This secured a massive star as the progenitor, despite the unusually large offset from the center of the host galaxy.
- A luminous radio counterpart peaking after ~ 20 d (rest frame) revealed the presence of a mildly relativistic outflow with bulk Lorentz factor $\Gamma > 1.6$ and energy $> 10^{48}$ erg (Bright et al. 2024).

This was the first such source discovered with this behavior, and was suggested as either a new class of transients or as providing the missing link between multiple known classes (e.g., van Dalen et al. 2024). The most promising interpretation is afterglow emission following a low luminosity GRB (Srivastav et al. 2024; Sun et al. 2024), although there is disagreement as to whether the XOIR SEDs are consistent with an afterglow origin (Srivastav et al. 2024; van Dalen et al. 2024). Srivastav et al. (2024) favored a refreshed shock origin for the second component, whereas van Dalen et al. (2024) argues that the SED was inconsistent with the X-ray and optical emission arising from the same process. Instead, van Dalen et al. (2024) favored a mildly relativistic outflow to create the X-ray and radio emission (see Bright et al. 2024), and the combination of a cocoon to produce the first component and the interaction between supernova ejecta and the circumstellar material (CSM) to produce the second component.

While the lack of gamma-ray emission, multiple optical emission components, long-lived and rather flat X-ray lightcurve, and luminous, late-peaking radio emission are all shared between EP240414a and EP241021a, the two events display some clear differences. For starters, the peak of the second component is significantly more luminous in EP241021a ($M_r \approx -21$ mag for EP240414a versus $M_r \approx -21.8$ mag for EP241021a), see Figure 5. In fact, due to its red color, EP241021a is even more extreme at near-infrared wavelengths ($M_J \approx -22.6$ mag). Furthermore, while EP240414a showed a clear third component which was spectroscopically confirmed

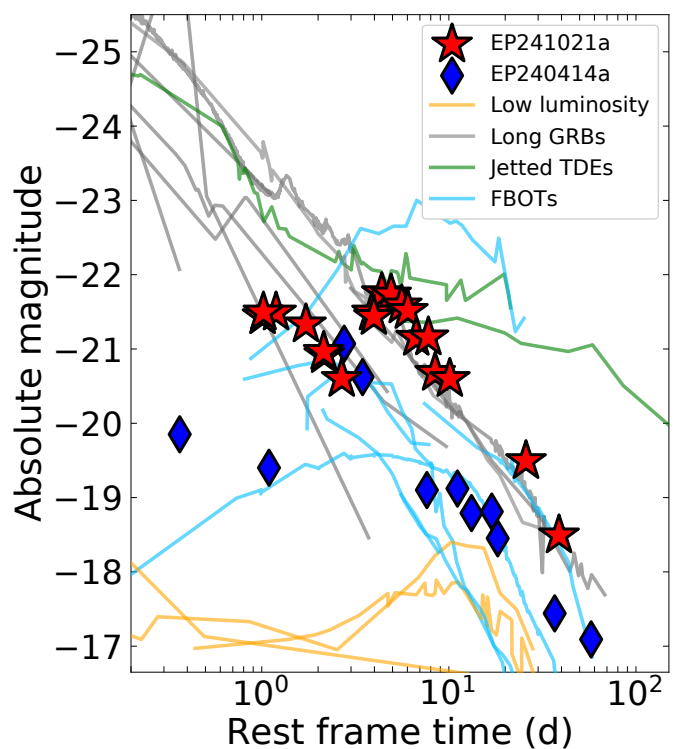


Fig. 5: Optical lightcurves (r -band) of a variety of fast optical transients (long GRBs, low luminosity GRBs, jetted TDEs, and FBOTs) compared to EP241021a (red stars) and EP240414a (blue diamonds; Srivastav et al. 2024; van Dalen et al. 2024; Sun et al. 2024). The low luminosity GRBs (orange) are supernova dominated over similar timescales, whereas EP241021a is nearly two magnitudes more luminous than any known GRB-SN (e.g., Hjorth & Bloom 2012; Cano et al. 2017), lying instead at similar absolute magnitudes to superluminous supernovae.

as a SN (van Dalen et al. 2024), typical of those seen in GRBs (Iwamoto et al. 1998; Galama et al. 1998), instead EP241021a is significantly more luminous by nearly 2 magnitudes (Figure 5).

In addition to the differing absolute magnitudes, the timescales of the optical lightcurve’s multiple components are significantly longer for EP241021a (Figure 5). These differences could be explained by outflows of different energies and Lorentz factors, especially in a refreshed shock model (see §4.7). Future discoveries of potentially similar events will aid in understanding the continuum of transient behavior linking these events, and potentially linking other classes of known transients. As we consider it likely these two events are of similar nature, and EP240414a is conclusively associated to the death of a massive star, albeit in a strange environment (e.g., van Dalen et al. 2024), we only consider a massive star progenitor scenario for EP241021a and do not explore other possible explanations (e.g., a tidal disruption event by an intermediate mass black hole).

4.3. Comparison to Other Fast Optical Transients

There is a diverse zoo of fast optical transients discovered by wide-field surveys in the last two decades. The classification of these transients is largely phenomenologically defined, without clear boundaries. These objects come from a variety of classes, but are regularly found to belong to either FBOTs (e.g., Drout et al. 2014; Vinkó et al. 2015; Pursiainen et al. 2018), “orphan”

GRB afterglows (e.g., Cenko et al. 2013; Law et al. 2018; Ho et al. 2023b, 2022; Lipunov et al. 2022; Mooley et al. 2022), or stripped-envelope supernovae (e.g., Yao et al. 2020; Clark et al. 2020; Das et al. 2024; Moore et al. 2024).

The distinction between FBOTs and other fast optical transients lies in their initially blue colors ($g-r < -0.2$ mag), initially featureless optical spectra, and luminous non-thermal X-ray and radio emission. Many FBOTs are found to display thermal optical emission (e.g., Perley et al. 2019), with some also having clearly non-thermal, self-absorbed radio emission out to more than a hundred days (e.g., Ho et al. 2020; Margutti et al. 2019). In Figure 5 we compare a zoo of optical transients to EP240414a and EP241021a. While FBOTs typically display optical emission with both fast rise ($< 2 - 5$ d) and decay timescales ($< 5 - 10$ d) that are consistent with EP240414a and EP241021a, the direct connection to FBOTs is unclear due to their different optical colors (red versus blue). As we do not find a direct analog to any previously known optical transients, we therefore explore other possible origins below.

4.4. Comparison to Dirty Fireballs and Orphan GRBs

Recent years have seen a variety of non-gamma-ray triggered GRB afterglow discoveries (e.g., Lipunov et al. 2022; Ho et al. 2022; Perley et al. 2024; Li et al. 2024a; Srinivasaragavan et al. 2025), largely through wide-field optical surveys such as the Zwicky Transient Facility (ZTF), though other attempts have been made (Freeburn et al. 2024b). These “orphan” afterglows (Nakar et al. 2002; Huang et al. 2002; Dalal et al. 2002; Totani & Panaitescu 2002; Levinson et al. 2002; Rhoads 2003) are generally observed as fast fading red transients and found at cosmological distances around $z \approx 1$ (e.g., Ho et al. 2022). A general issue, due largely to the lack of direct knowledge of the onset time of the initial GRB or afterglow, is whether these events truly lack gamma-ray emission, whether it was simply missed by gamma-ray monitors, or whether the gamma-ray emission is simply underluminous or having a low peak energy E_p . They are often suggested to be mildly relativistic outflows (e.g., Perley et al. 2024; Li et al. 2024a; Srinivasaragavan et al. 2025), candidate dirty fireballs (Rhoads 2003), though slightly off-axis viewing angles cannot be ruled out as an alternative explanation (e.g., Li et al. 2024a).

The clearly non-thermal emission at X-ray, OIR, and radio wavelengths produced by EP241021a is suggestive of the afterglow of a relativistic jet (e.g., Granot & Sari 2002). Therefore, drawing a connection to these “orphan” GRBs that are also lacking gamma-rays is natural. As these events were detected prior to the launch of EP, it is difficult to rule out that they also produced soft energy X-ray emission. A GRB can lack gamma-ray emission for a few reasons, most naturally being a viewing angle θ_{obs} outside of the jet’s core half-opening angle θ_c or a low Lorentz factor (see, e.g., O’Connor et al. 2024, for a discussion). It is thought that non-gamma-ray triggered events may trace a continuum of outflow Lorentz factors, potentially caused by a continuum of failed stellar explosions (i.e., where the jet breaks out of the progenitor star with varying success). Future observations of these events, especially coincident with EP triggers, is critical to understand this possible continuum. In what follows we consider possible GRB afterglow origins for EP241021a.

4.5. The Prompt Emission

The high energy detection of EP241021a and the non-thermal SED are reminiscent of cosmological gamma-ray bursts, which are the most commonly observed class of high-energy transients. As such, we compare the high energy properties of EP241021a to typical gamma-ray bursts. In Figure 6 (left panel), we show the approximate isotropic-equivalent $0.5 - 4$ keV energy released by EP241021a during the initial EP trigger (§2.1; Hu et al. 2024) versus different classes of gamma-ray bursts. The non-detection of EP241021a by *Konus-Wind* (§2.1) is easily explained if the peak energy E_p is low, as was the case for EP240414a (Sun et al. 2024). In comparing the reported photon indices based on power-law spectral fits to the EP triggers (Hu et al. 2024; Sun et al. 2024), the spectrum of EP241021a ($\Gamma = -1.5 \pm 1.2$ at 90% CL; consistent with a non-thermal spectrum) appears substantially harder than EP240414a ($\Gamma = -3.1 \pm 0.8$ at 1σ CL; Sun et al. 2024) which had an extremely low peak energy $E_p < 1.3$ keV (Sun et al. 2024), an outlier for a gamma-ray burst. Instead, EP241021a does not require such a low peak energy to be consistent with the non-detection of prompt gamma-ray emission (see also O’Connor et al. 2025). Using the energy constraints from *Konus-Wind* (Figure 6), we determine that for a typical long GRB spectrum ($\alpha = -1$ and $\beta = -2.5$) extrapolating the prompt EP trigger ($0.5 - 4$ keV) with a standard bolometric correction requires $E_p \lesssim 100$ keV to not overproduce the *Konus-Wind* limits ($1 - 10,000$ keV) for the same spectral shape. This is a reasonable limit to the peak energy and consistent with the values observed for many long GRBs and their location on the Amati relation which conservatively suggests $E_p \lesssim 20$ keV (e.g., Amati 2006).

In any case, the general energetics of these two events clearly lie within those of the class of low luminosity GRBs (e.g., Iwamoto et al. 1998; Galama et al. 1998, 1999; Malesani et al. 2004; Sakamoto et al. 2004; Soderberg et al. 2004a,b, 2006; Ofek et al. 2007; Starling et al. 2011; Cano et al. 2011; D’Elia et al. 2018; Izzo et al. 2019; H. E. S. S. Collaboration et al. 2021; Dichiaro et al. 2022; Irwin & Hotokezaka 2024c), which could be easily missed by *Konus-Wind* depending on the uncertain spectral shape of the prompt emission. On the other hand, the X-ray emission has more luminous long-lived plateaus than observed in other low luminosity GRBs (Figure 6; right panel), e.g., GRB 171205A (D’Elia et al. 2018). Moreover, the optical lightcurve (Figure 5) is significantly different from the typically supernova dominated lightcurves of low luminosity GRBs (e.g., Soderberg et al. 2006; Starling et al. 2011; Cano et al. 2011; D’Elia et al. 2018; Izzo et al. 2019).

We note that the observed X-ray plateaus from EP240414a and EP241021a do appear to be consistent with an extension of the typical rest-frame GRB X-ray plateau correlations between luminosity and duration (Figure 7; e.g., Dainotti et al. 2008; Tang et al. 2019; Xu et al. 2021), which supports the interpretation of EP240414a and EP241021a in the context of GRBs. Due to their sparsely sampled X-ray lightcurves, when compared to typical GRBs (Figure 6; right panel), we display the allowed range of X-ray plateau luminosity and duration as shaded regions. The exact end time of the plateau is not well constrained for either source. These shaded regions (Figure 7) appear consistent with extrapolating the observed behavior of GRBs to lower luminosities and longer durations. If confirmed, these would be the longest plateaus detected from a GRB-like outflow.

Both the energetics and X-ray emission are significantly higher than found for the FXTs discovered prior to the launch of EP (e.g., Alp & Larsson 2020; Quirola-Vázquez et al. 2022,

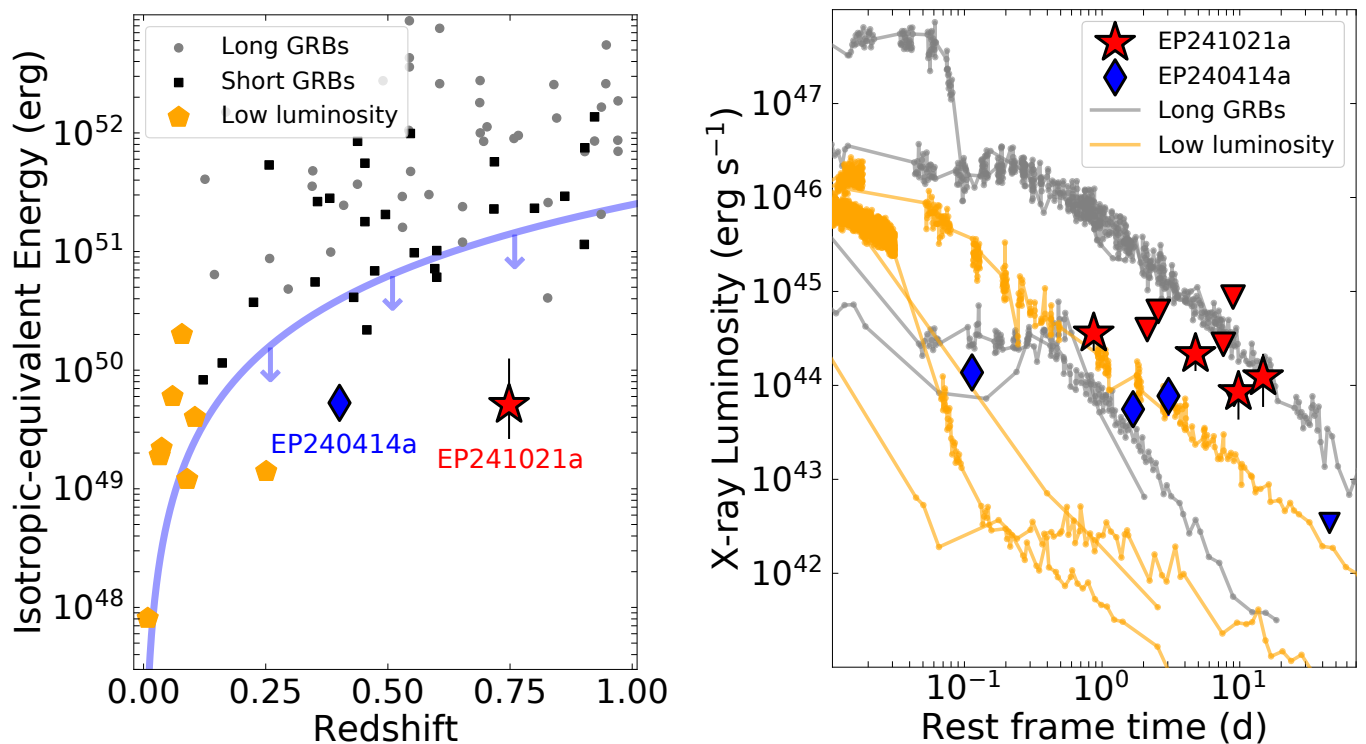


Fig. 6: **Left:** Isotropic-equivalent gamma-ray energies (1 – 10,000 keV) of both short (black squares) and long duration (gray circles) GRBs versus redshift (Sakamoto et al. 2011; Lien et al. 2016; Atteia et al. 2017; O’Connor et al. 2024). A population of low luminosity GRBs is shown by orange pentagons (e.g., Iwamoto et al. 1998; Galama et al. 1998, 1999; Malesani et al. 2004; Sakamoto et al. 2004; Soderberg et al. 2004a,b, 2006; Ofek et al. 2007; Starling et al. 2011; Cano et al. 2011; D’Elia et al. 2018; Izzo et al. 2019; H. E. S. S. Collaboration et al. 2021; Dichiaro et al. 2022). The approximate energy release (0.5 – 4 keV) of the initial EP detection of EP241021a is shown as a red star (§2.1; Hu et al. 2024). For comparison, EP240414a is also shown as a blue diamond (Sun et al. 2024). The blue line shows the gamma-ray limits from *Konus-Wind* as a function of redshift for comparison to the larger population of high-energy transients. **Right:** Rest frame X-ray lightcurves of *Swift* long GRBs (gray) and low luminosity GRBs (orange) compared to the combined FXT and XRT lightcurves of EP241021a and EP240414a (Sun et al. 2024; van Dalen et al. 2024).

2023) suggesting a separation between the two classes, or, potentially, a continuum. The lack of clear multi-wavelength detections of pre-EP FXTs complicates this connection. Further observations of EP transients are required before drawing strong conclusions regarding any potential connection to classical pre-EP FXTs.

4.6. Constraints on the Initial Lorentz Factor

4.6.1. Lorentz Factor Limits from the Prompt Emission

The prompt emission spectrum observed by EP appears consistent with non-thermal emission ($\Gamma = -1.5 \pm 1.2$ at 90% CL; Hu et al. 2024), though there is significant uncertainty on the true photon index. Producing a non-thermal, likely synchrotron, spectrum requires that the energy is dissipated at a radius that is at least as large as the photosphere of the outflow (e.g., Goodman 1986; Thompson 1994). Thus, we require that the emission occurs at a low optical depth $\tau \lesssim 1$. Based on the EP trigger, a minimum energy release is 5×10^{49} erg (0.5 – 4 keV) over the $t_{\text{dur}} \sim 100$ s trigger (Hu et al. 2024), which is potentially much higher in larger energy bands. In addition, the true isotropic kinetic energy of the outflow is also likely much larger when accounting for radiation efficiency, and likely exceeds $E_{\text{kin}} \gtrsim 10^{50}$ erg. If the source is non-relativistic then $E_{\text{kin}} = E_{\text{kin,true}} \sim Mv^2/2$

and the radius as a function of time for a given outflow velocity v is given by $R \sim vt$. The optical depth of the outflow to Thomson scattering is then $\tau \sim 2\kappa E_{\text{kin}}/(v^4 t_{\text{dur}}^2)$ where κ is the opacity. As the optical depth decreases rapidly with an increase in velocity, we conservatively assume a non-relativistic outflow ($v \sim 0.75c$, such that $\Gamma_0 < 1.5$ and relativistic effects can be ignored), which produces an extremely high optical depth of order hundreds. This would produce a thermal spectrum in sharp contrast to the observed prompt X-ray spectrum.

The optical depth can be decreased by assuming a higher velocity outflow. Expanding this calculation to the transrelativistic case, the optical depth is given by

$$\tau = 100 \frac{(\Gamma - 1)E_{50}}{\Gamma_0^4 \beta^2 t_{\text{dur},2}^2}, \quad (1)$$

where we have applied the convention that $E_{50} = E/(10^{50}$ erg) is the isotropic-equivalent energy and $t_{\text{dur},2} = t_{\text{dur}}/(100$ s) is the prompt emission duration. By requiring $\tau < 1$, we find an initial bulk Lorentz factor of $\Gamma_0 \gtrsim 4$. If instead the isotropic-equivalent energy were higher, we would likewise require a larger Lorentz factor. While we cannot rule out efficient dissipation in the mildly optically thick regime with at τ of a few, these calculations provide support for at least a mildly relativistic outflow to produce the prompt X-ray trigger of EP241021a.

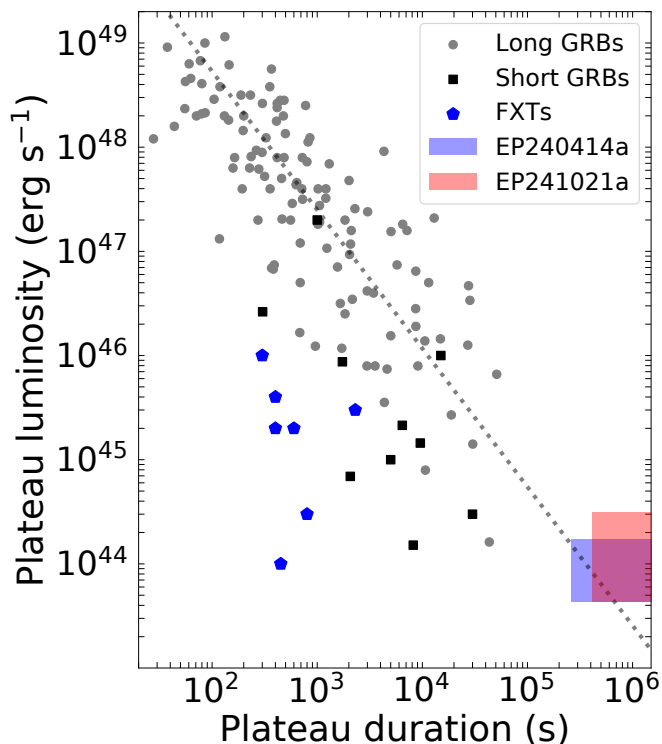


Fig. 7: Observed X-ray plateau rest frame duration and luminosity for GRBs (Tang et al. 2019; Xu et al. 2021) and FXTs (Quirola-Vásquez et al. 2024) versus EP240414a (blue shaded region) and EP241021a (red shaded region). The dotted line is shown to guide the eye and extend the GRB plateau correlation.

4.6.2. Lorentz Factor Limits from Jet Deceleration

If we assume the multi-wavelength emission from EP241021a is related to the interaction of a relativistic jet with its surrounding environment we can constrain the initial bulk Lorentz factor of the outflow. For an on-axis observer, the afterglow emission will be observed to be declining after the jet has decelerated (see, e.g., O’Connor et al. 2020, 2024, for a discussion of the impact of the viewing angle). Therefore, based on the declining optical lightcurve starting at 1.14 d (0.65 d in the rest frame; Zheng et al. 2024b), we can set a lower limit to the initial bulk Lorentz factor Γ_0 of material at the jet’s core. A relativistic jet propagating into an external environment $\rho(r) \propto r^{-k}$, where $k=0$ represents a uniform density environment and $k=2$ for a stellar wind environment, begins to decelerate after a dynamical timescale t_{dec} given by (Sari & Piran 1999; Molinari et al. 2007; Ghisellini et al. 2010; Ghirlanda et al. 2012; Nava et al. 2013; Nappo et al. 2014; Ghirlanda et al. 2018)

$$\frac{t_{\text{dec}}}{1+z} = \left(\frac{17-4k}{16\pi(4-k)} \frac{E_{\text{kin}}}{c^{5-k} A \Gamma_0^{8-2k}} \right)^{1/(3-k)}, \quad (2)$$

where Γ_0 is the initial bulk Lorentz factor at the jet’s core, E_{kin} is the kinetic energy, $A = m_p n_0 R_0^k$, n_0 is the density, m_p is the proton mass, and c is the speed of light. Equation 2 simplifies to

$$\frac{t_{\text{dec}}}{1+z} \lesssim \begin{cases} 0.68 \Gamma_{0,1}^{-8/3} E_{\text{kin},52}^{1/3} n^{-1/3} \text{ d} & k=0, \\ 0.76 \Gamma_{0,1}^{-4} E_{\text{kin},52} A_{*,1}^{-1} \text{ d} & k=2, \end{cases} \quad (3)$$

where $E_{\text{kin},52} = E_{\text{kin}}/(10^{52} \text{ erg})$, $\Gamma_{0,1} = \Gamma_0/10$, and $A_* = n_0 R_0^2/(3 \times 10^{35} \text{ cm}^{-1})$ with $R_0 = 10^{18} \text{ cm}$ such that $A_{*,1} = A_*/0.1$. The con-

straint on the Lorentz factor is degenerate with the kinetic energy of the blastwave and the density of the surrounding environment, but roughly we can assume lower limits to the Lorentz factor in the range $\Gamma_0 \gtrsim 5 - 10$ to be reasonable. It is important to note that there are no robust constraints on the exact start time of the jet’s deceleration, and as such it is rather unconstrained and an extremely early deceleration, typical of cosmological GRBs, cannot be excluded.

4.7. Possible origins of EP241021a

4.7.1. A Rare Supernova

Motivated by the similarities of the second bump to the timescale of FBOTs and the peak absolute magnitudes of superluminous supernovae (SLSN), we consider a range of supernova-like models that have been applied to both classes of events. We note that none of these models naturally explains the fast multi-peaked lightcurve of EP241021a (Figure 2) without an added component. As such, we consider only the data corresponding to the rebrightening phase.

We used the Modular Open Source Fitter for Transients (MOSFiT; Nicholl et al. 2017; Guillochon et al. 2018) to fit the OIR lightcurve shown in Figure 2. Motivated by possible explanations for the most luminous supernovae, we consider models that include the decay of ^{56}Ni , the spin-down of a magnetar, and CSM interactions. We compare the fitted lightcurves, and analyze potential explanations for the morphology of the second component in the light curve (> 6 d; observer frame). We applied five different MOSFiT models: *i*) default (Nadyozhin 1994), *ii*) csm (Chatzopoulos et al. 2013; Villar et al. 2017), *iii*) csmni, *iv*) magnetar (Nicholl et al. 2017), and *v*) magni. The csmni and magni models combine their respective basic engines and the default model. The default model is based on the radioactive decay of ^{56}Ni being the main source of the lightcurve morphology.

To fit the second component starting from MJD = 60609.81, we fix the explosion time to the EP trigger, such that $t_{\text{exp}} = -5.60$ days prior to the onset of the rebrightening. The γ -ray opacity (κ_γ) was fixed to $0.027 \text{ cm}^2 \text{ g}^{-1}$ (Cappellaro et al. 1997). We perform the fit using the dynamic nested sampling approach implemented in MOSFiT using the dynesty package (Speagle 2020; Koposov et al. 2024). For the magnetar model, we set similar priors as Gomez et al. (2022) to model superluminous supernovae, but decreased the range of the magnetar spin period to $P_{\text{spin}} \in [0.7, 10]$ ms. Instead of log-flat priors for f_{Ni} , v_{ej} , and B_\perp we chose a flat prior. For csm and csmni, we apply similar priors as in Nicholl et al. (2020); Suzuki et al. (2021); Chen et al. (2023). For a more detailed overview of the priors for each model see C.1. Relevant posteriors are listed in C.2.

Within a general supernova framework where the decay of ^{56}Ni serves as the primary energy source, the Arnett (1982) model primarily fits two parameters: the ejecta mass M_{ej} of ^{56}Ni and the characteristic diffusion timescale τ_{diff} . Here, τ_{diff} governs the width of the light curve, and is determined as

$$\tau_{\text{diff}}^2 = \frac{2\kappa_{\text{opt}} M_{\text{ej}}}{\beta c v_{\text{ej}}}, \quad (4)$$

with κ_{opt} , c , v_{ej} , and β being the optical opacity, the speed of light, and the bulk velocity of the ejected material, and a constant (Arnett 1982), respectively. In order to match the observed lightcurve, we need to achieve an extreme luminosity ($M_r \approx -22$ mag), while still maintaining a fast evolution of

the OIR lightcurve’s rising and declining phases. According to Equation 4, a low ejected bulk mass and/or a high velocity of the ejected material would contribute to a rapid evolution in the light curve. However, it can be challenging to obtain rapidly evolving, luminous transients when including the contribution of ^{56}Ni decay.

In Figure 8, we display the best fit to this second component of the lightcurve for each of the five MOSFiT models. While we have performed these fits to the multi-band lightcurve, we display the fit results only for the best sampled band – the r -band – for readability purposes and to avoid a cluttered figure. Each color in Figure 8 represents a single model applied to the data compared to the r -band lightcurve. We find that none of these models are capable of reproducing the observed shape (even for extreme parameters), and, furthermore, none of them would capture the initial decaying phase at < 6 d. The closest match comes from the `csmni` model, but this predicts a much slower decay, and, importantly, this model significantly overpredicts the late time r -band photometry.

These MOSFiT models are based on cooling thermal emission, and are based on the assumption that the OIR spectral energy distribution is well matched to the shape of a blackbody. In Figure 8 we have only shown the model fits to the r -band, despite having modeled the multi-band lightcurves. Due to the underlying assumption of a cooling blackbody, the model fits (default, magnetar, and magni) to the other bands are quite poor and do not provide a good match to the lightcurves. On the other hand, the `csmni` and `csm` models can provide a rough match to the post-peak behavior in all bands (similar to that shown in Figure 8 for the r -band). However, in order to match the observed non-thermal spectral shape of EP241021a ($F_\nu \propto \nu^{-1}$; Figure 4), the `csmni` and `csm` in MOSFiT require large amounts of dust ($A_V \gtrsim 1.5$ mag) that push the transient to extreme absolute magnitudes ($\lesssim -23.5$ to -24.5 mag) that are not observed from supernovae. For example, the most luminous SLSNe peak at $M_r \sim -22.7$ (e.g., DES16C2nm, SCP06F6; Gomez et al. 2024), and these are already significant $\sim 2\sigma$ outliers from the rest of the population (e.g., Gomez et al. 2024).

In addition to not performing well to fit the light curves (and still requiring an additional component at early times), multiple other arguments provide evidence against a SLSN interpretation, including the fast timescale, red color (whereas SLSNe are initially blue $g - r \approx -0.2$; Gomez et al. 2024), non-thermal SED, and lack of clear SN features in the optical spectra (§2.3; Pugliese et al. 2024; Pérez-Fournon et al. 2024; Zheng et al. 2024a). Moreover, the luminous non-thermal radio emission observed from EP241021a ($\sim 10^{31}$ erg cm $^{-2}$ s $^{-1}$ Hz $^{-1}$; Yadav et al., in preparation) is in sharp contrast to observations of SLSNe which show no radio emission to depths between $\sim 1 - 4$ orders of magnitude lower (e.g., Copejans et al. 2018; Eftekhari et al. 2019).

4.7.2. An Off-axis Structured Jet

The clearly double peaked optical and near-infrared lightcurve (Figure 2) is not observed in standard GRB afterglows. However, Beniamini et al. (2020, 2022) showed that double-peaked afterglow lightcurves can be produced by a combination of line-of-sight material (producing the first peak) and the jet’s core emission (producing the second peak). The major factor dictating whether an observer views a single or double peaked lightcurve is the lowest latitude of the jet θ_* , from which material is initially beamed towards the observer ($\theta_*\Gamma(\theta_*) = 1$; see discussions in Beniamini et al. 2020, 2022 and Figure 8 of Beniamini et al.

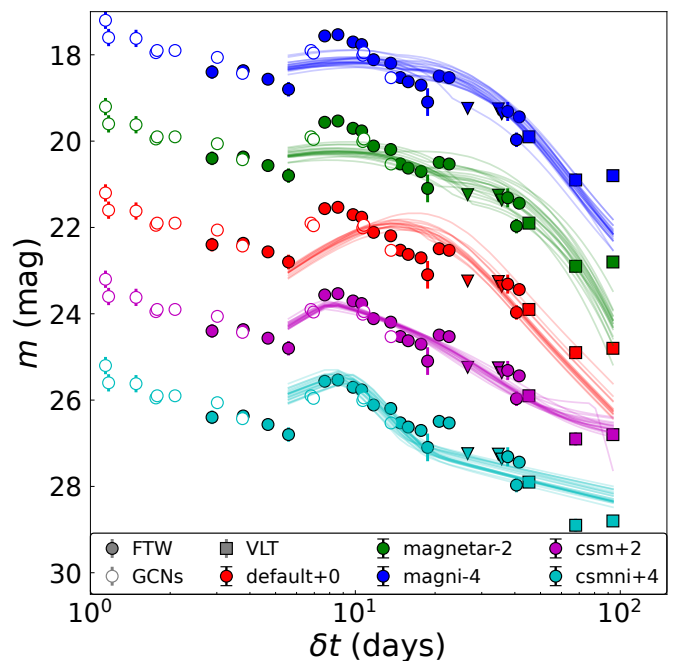


Fig. 8: Comparison between supernova models and the observed optical lightcurve. The best fits to the second component are shown for a range of MOSFiT models (default, magnetar, magni, csm, and csmni; see §4.7.1) in r -band. The model fits to the other filters (z and J) are either quite poor, or require large amounts of dust.

2022). If $\theta_{\text{obs}} > \theta_*$ then the the observer is continuously receiving emission from decreasing angles until finally observing the core, producing a single peaked lightcurve. The alternative case, where $\theta_{\text{obs}} < \theta_*$ produces a double peaked lightcurve as initially the observer is viewing material far away from the core that will decelerate before the observer is able to receive emission from the core (due to relativistic beaming), producing a first peak at approximately $t_{\text{dec}}(\theta_{\text{obs}})$ (see, e.g., O’Connor et al. 2024). The secondary peak occurs once the core is de-beamed to the observer, and is the more standard peak for off-axis GRBs in the literature (e.g., GW170817; Mooley et al. 2018; Ghirlanda et al. 2019; Ryan et al. 2023). The relative significance of the second peak is dictated by the slope of the structured jet with $E(\theta) \propto \theta^{-a}$. Steeper jets and a uniform density environment serve to substantially pronounce the second peak (see Figure 11 of Beniamini et al. 2022). While this may be able to match the timescale and flux ratio of the double peaked lightcurve, the observed rise to the second peak is too steep to naturally fit with this interpretation. We therefore disfavor a forward shock from an off-axis structured jet as the cause of EP241021a’s rebrightening.

However, an alternative possibility is that the rebrightening is due to a reverse shock from off-axis material in a shallow structured jet (e.g., O’Connor et al. 2023; Gill & Granot 2023; Zhang et al. 2024). This does not necessarily require an off-axis viewing angle for the observer. Material at an off-axis angle would be moving with lower Lorentz factors and also be delayed with regard to photons reaching the observer (due to relativistic beaming). This may provide a natural explanation for the observed delayed brightness increase in EP240414a and EP2141021a. Recently Abdikamalov & Beniamini (2025) performed a comprehensive investigation of the possible lightcurve behaviors of reverse and forward shock emission for steep off-axis jets. They

found a variety of possible double-peaked lightcurve profiles, due to de-beamed emission from the reverse shock. Future work will extend these considerations to shallow structured jets, and may reveal the capability to reproduce the observed behavior of EP241021a due to emission from a reverse shock from an off-axis angle.

4.7.3. A Refreshed Shock

Over the past two decades observations of GRBs have revealed a variety of peculiar, unexpected late-time behaviors. These include long-lived X-ray (e.g., Zhang et al. 2006; Troja et al. 2007) and optical (Panaitescu & Vestrand 2011; Knust et al. 2017) plateaus, late-time X-ray (Burrows et al. 2005b; Curran et al. 2008; Margutti et al. 2011; Bernardini et al. 2011) and optical (Swenson et al. 2013; Kumar et al. 2022) flares, and rapid episodes of rebrightening (e.g., Covino et al. 2008; Melandri et al. 2014; Dichiara et al. 2022; Moss et al. 2023). In many cases these phenomena have been attributed to long-lived central engine activity (Burrows et al. 2005b; Zhang et al. 2006; Curran et al. 2008; Margutti et al. 2011), but other explanations are plausible (Panaitescu 2008; Beniamini & Kumar 2016; Beniamini & Mochkovitch 2017; Lamberts & Daigne 2018; Ayache et al. 2020; Duque et al. 2022).

Late-time rebrightening is often attributed to refreshed shocks (Rees & Mészáros 1998; Sari & Mészáros 2000; Kumar & Panaitescu 2000; Jóhannesson et al. 2006), such as observed in the afterglows of GRBs 030329 (Granot et al. 2003; Moss et al. 2023), 071010A (Covino et al. 2008), GRB 120326A (Melandri et al. 2014), and GRB 160821B (Lamb et al. 2019), among others, though in some cases a reverse shock is also possible (e.g., Dichiara et al. 2022). We note that extreme rebrightening episodes have also been observed in X-ray flashes (XRFs) such as XRF 050416a (Soderberg et al. 2007) at ~ 25 d (rest frame), which may also have been due to a refreshed shock. In the standard refreshed shock model (Sari & Mészáros 2000; Kumar & Panaitescu 2000), promptly launched and rapid ($\Gamma_0 \gtrsim 100$) material decelerates as it sweeps up circumburst material in an external shock at the front of the outflow, eventually becoming slow enough for an initially less relativistic shell ($\Gamma_0 \lesssim 10 - 20$) to catch up and merge into a single blastwave, producing the increase in brightness, which is related to the energy added to the shock.

However, the rebrightening observed in EP241021a is at significantly later times ($\sim 6.5 \times 10^5$ s; observer frame), and is difficult to obviously connect to the behavior observed in on-axis cosmological GRBs, especially in terms of the relative significance of the rebrightening (i.e., by more than a magnitude). The time of the rebrightening can be related to the time of the shell collision when $\Gamma_f(t_{\text{coll}}) = \Gamma_{0,s}/2$, which in a uniform density environment occurs at (Moss et al. 2023):

$$t_{\text{coll}} = 6.8 \times 10^5 \text{ s} \left(\frac{1+z}{1.75} \right) \left(\frac{E_{\text{kin}}}{10^{53} \text{ erg}} \right)^{1/3} \left(\frac{n}{1 \text{ cm}^{-3}} \right)^{-1/3} \left(\frac{\Gamma_s}{6} \right)^{-8/3} \quad (5)$$

This timescale occurs for $\Gamma_s \approx 6$ if the (isotropic-equivalent) kinetic energy is $\sim 10^{53}$ erg, which is likely on the extreme end of the possible values. If instead we consider a lower energy of $\sim 10^{51}$ erg with fixed density $n = 1 \text{ cm}^{-3}$, the Lorentz factor of the slower moving material is then $\Gamma_s \approx 3$ due to the rather weak dependence on energy in Equation 5. Instead, in a wind environment, where $t_{\text{coll}} \propto (E_{\text{kin}}/A_*) \Gamma_s^{-4}$ (Moss et al. 2023), we find $\Gamma_s \approx 7(2)$ for $E_{\text{kin}} \sim 10^{53} (10^{51})$ erg. Regardless, in either case,

the trailing ejecta would have to at least be mildly relativistic, requiring that the initial outflow is also relativistic.

The rebrightening timescale of EP241021a is consistent with $\Delta t_{\text{coll}}/t_{\text{coll}} \lesssim 0.3$, similar to the observations of GRB 030329 (Granot et al. 2003; Moss et al. 2023). To good approximation, the rise time is the same as the reverse shock (RS) crossing time (Sari & Piran 1995), which is determined by the ratio of Lorentz factors (e.g., Moss et al. 2023) such that $\Delta t_{\text{coll}}/t_{\text{coll}} \approx \Delta \Gamma_s/\Gamma_s$ to order unity corrections, where $\Delta \Gamma_s$ is the difference in Lorentz factors across the slower moving ejecta shell. We do not consider either a density enhancement (e.g., Ramirez-Ruiz et al. 2001; Dai & Lu 2002; Nakar et al. 2003; Nakar & Granot 2007; van Eerten et al. 2009), or complex density profile (potentially due to the progenitor star's mass loss history), or long-lived central engine activity to explain the rebrightening, as none of these explanations are capable of easily producing the variability timescale ($\Delta t/t \lesssim 0.3$) and extremely steep rise required by the rebrightening of the OIR afterglow (steeper than $t^{3.2}$ at 90% CL; see §3.1).

The OIR temporal and spectral indices (§3.1 and §3.2) are capable of matching standard afterglow closure relations for either a uniform density or wind environment (Granot & Sari 2002). In a wind environment, as expected for a massive star progenitor, the X-ray, optical, and near-infrared data would be above the cooling frequency ($\nu_c < \nu$) such that the temporal index and spectral index are $\alpha = (2 - 3p)/4 = -1.15$ and $\beta = -p/2 = -1.10$ for $p = 2.2$ (Granot & Sari 2002). These indices are roughly consistent with the values inferred in §3.1 and §3.2. We note that for emission above the cooling frequency the closure relation is unchanged between a uniform density or wind environment. An additional possibility for a uniform density environment is a steep value of $p \approx 3$ such that $\beta = (1 - p)/2 = -1$ and $\alpha = 3(1 - p)/4 = -1.5$. While the temporal slope has a better match for $p \approx 2.5$, it is less consistent with the observed spectral index. In either scenario, the radio data is below the injection frequency $\nu_R < \nu_m < \nu_c$ (Yadav et al., in preparation).

The refreshed shock interpretation naturally explains the steep rise observed at OIR wavelengths (Figure 5), as well as the flat X-ray lightcurve⁵ (Figure 6; right panel). A refreshed relativistic shockwave produces a non-thermal spectrum that provides a better description of the data than CSM interaction with non-relativistic supernova ejecta, which is commonly thought to produce a blackbody-like spectrum that is not observed (see Figure 4 and §4.7.1). Moreover, the possible consistency between the early and late temporal slopes α_1 and α_2 with $\alpha_1 = \alpha_3 = -1.15 \pm 0.04$ (see §3.1 for details) is suggestive of the refreshed shock scenario, as other models would not necessarily produce such behavior without fine tuning.

As our data do not show a clear jet-break out to late-times ($t_j \gtrsim 100$ d; observer frame), we can set a constraint on the opening angle of the jet. Assuming an on-axis jet, the jet's half-opening angle is larger than (Sari et al. 1999; Rhoads 1999; Frail

⁵ In this scenario where the X-ray and optical behavior is linked to the same emission mechanism or outflow, then the observed X-ray lightcurve is not a true plateau (only appearing so due to the sparse X-ray data), and would not apply in the manner shown in Figure 7. Higher cadence (and higher signal-to-noise) X-ray data is required for future events to either prove or disprove this hypothesis.

et al. 2001; Chevalier & Li 2000; Bloom et al. 2003):

$$\theta_c = \begin{cases} 0.31 \text{ rad} \left(\frac{t_j}{100 \text{ d}} \right)^{3/8} \left(\frac{E_{\text{kin}}}{10^{52} \text{ erg}} \right)^{-3/8} \left(\frac{n}{10^{-2} \text{ cm}^{-3}} \right)^{3/8}, & k = 0, \\ 0.18 \text{ rad} \left(\frac{t_j}{100 \text{ d}} \right)^{1/4} \left(\frac{E_{\text{kin}}}{10^{52} \text{ erg}} \right)^{-1/4} \left(\frac{A_*}{10^{-2}} \right)^{1/4}, & k = 2. \end{cases} \quad (6)$$

where we have already applied the redshift corrections using $z = 0.75$. Not unexpectedly given the late time of any jet break, these half-opening angles are rather large, for a GRB jet, especially for $k = 0$ where $\theta_c \gtrsim 20$ deg, but they are not completely unprecedented (e.g., Frail et al. 2001; Wang et al. 2018; Rouco Escorial et al. 2022; O'Connor et al. 2023). However, different assumptions for the kinetic energy and density can decrease this opening angle slightly. As the trailing ejecta is likely more collimated than the initial outflow, a larger angle more easily favors the production of a rebrightening episode with $\Delta t_{\text{coll}}/t_{\text{coll}} \lesssim 0.3$; see Moss et al. (2023) for a discussion.

However, a weakness of the refreshed shock model is the lack of similar rebrightening in the optical lightcurves of on-axis cosmological GRBs. Figure 5 shows EP241021a is at the extreme end of GRB optical luminosities, and comparable to the brightest-of-all-time GRB 221009A at a similar timescale (e.g., O'Connor et al. 2023; Laskar et al. 2023). Such behavior would be hard to miss in past GRBs, implying that EP240414a and EP241021a would have unique central engine properties, potentially resulting from either a failed or marginally successful jet breakout, which can also explain the lack of gamma-rays. As EP240414a and EP241021a are clearly different from typical GRBs, it is possible that other properties of their outflows are atypical, such as their Lorentz factors being mildly relativistic and the presence of trailing ejecta with sufficient energy to lead to a significant bump. Further exploration of the detectability of similar refreshed shocks in typical cosmological GRBs is left for future work, and will aid in determining the uniqueness of this refreshed shock model for EP241021a.

5. Conclusions

We have presented the results of our multi-wavelength follow-up campaign of EP241021a over the first 100 days of its evolution, including long-term monitoring with the FTW, VLT, and HET. Here, we summarize our main conclusions:

- We determine that both EP241021a and EP240414a are likely produced by the same type of progenitor system, which is related to the death of a massive star.
- The non-thermal prompt soft X-ray emission detected by EP requires at least a mildly relativistic outflow with bulk Lorentz factor $\Gamma \gtrsim 4$. This interpretation is supported by the luminous radio emission (Yadav et al., in preparation).
- The lack of gamma-rays may be due either to the limited sensitivity of the available gamma-ray telescopes, a low peak energy E_p , or a low gamma-ray efficiency, potentially caused by a low outflow Lorentz factor.
- The rapid optical rebrightening (Figure 2) is challenging to explain with supernova-like models (Figure 8), but may be related to either refreshed shocks or a reverse shock from off-axis material. In either scenario we favor a mildly relativistic outflow producing non-thermal synchrotron radiation.

Future observations of similar events are required to build a sample, which will aid in determining the progenitor system,

emission mechanisms, and diversity of their outflows. In particular, a refined X-ray dataset and multi-wavelength observations at < 1 d would provide strong constraints on the available models and the onset of the first component and its Lorentz factor.

Acknowledgements. M. B. is supported by a Student Grant from the Wübben Stiftung Wissenschaft. B. O. is supported by the McWilliams Postdoctoral Fellowship at Carnegie Mellon University. P. B. is supported by a grant (no. 2020747) from the United States-Israel Binational Science Foundation (BSF), Jerusalem, Israel, by a grant (no. 1649/23) from the Israel Science Foundation and by a grant (no. 80NSSC 24K0770) from the NASA astrophysics theory program. M. M.'s research was supported by an appointment to the NASA Postdoctoral Program at the NASA Goddard Space Flight Center, administered by Oak Ridge Associated Universities under contract with NASA. E. T., Y.-H. Y., and M. Y. are supported by the European Research Council through the Consolidator grant BHianca (grant agreement ID 101002761). This paper contains data obtained at the Wendelstein Observatory of the Ludwig-Maximilians-University Munich. This research has made use of the XRT Data Analysis Software (XRTDAS) developed under the responsibility of the ASI Science Data Center (ASDC), Italy. This research has made use of data and/or software provided by the High Energy Astrophysics Science Archive Research Center (HEASARC), which is a service of the Astrophysics Science Division at NASA/GSFC. This paper contains data from observations obtained with the Hobby-Eberly Telescope (HET), which is a joint project of the University of Texas at Austin, the Pennsylvania State University, Ludwig-Maximilians-Universität München, and Georg-August Universität Göttingen. The HET is named in honor of its principal benefactors, William P. Hobby and Robert E. Eberly. We thank Cassie Crowe, Nathan McReynolds, Stephen Odewahn, Justen Pautzke, Amy Ray, Sergey Rostopchin and Amy Westfall from the HET staff for obtaining the observations. We acknowledge the Texas Advanced Computing Center (TACC) at The University of Texas at Austin for providing high performance computing, visualization, and storage resources that have contributed to the results reported within this paper. The Low Resolution Spectrograph 2 (LRS2) was developed and funded by the University of Texas at Austin McDonald Observatory and Department of Astronomy, and by Pennsylvania State University. We thank the Leibniz-Institut für Astrophysik Potsdam (AIP) and the Institut für Astrophysik Göttingen (IAG) for their contributions to the construction of the integral field units. This research has made use of the Astrophysics Data System, funded by NASA under Cooperative Agreement 80NSSC21M00561. This research has made use of adstex (<https://github.com/yymao/adstex>). This work made use of the catalog presented by Dainotti et al. (2024). This work made use of the Astro-COLIBRI platform (Reichherzer et al. 2021).

References

- Abdikamalov, E. & Beniamini, P. 2025, arXiv e-prints, arXiv:2502.12757
- Alp, D. & Larsson, J. 2020, ApJ, 896, 39
- Amati, L. 2006, MNRAS, 372, 233
- Appenzeller, I., Fricke, K., Fürtig, W., et al. 1998, The Messenger, 94, 1
- Arnett, W. D. 1982, ApJ, 253, 785
- Attea, J. L., Heussaff, V., Dezalay, J. P., et al. 2017, ApJ, 837, 119
- Ayache, E. H., van Eerten, H. J., & Daigne, F. 2020, MNRAS, 495, 2979
- Band, D., Matteson, J., Ford, L., et al. 1993, ApJ, 413, 281
- Beniamini, P., Gill, R., & Granot, J. 2022, MNRAS, 515, 555
- Beniamini, P., Granot, J., & Gill, R. 2020, MNRAS, 493, 3521
- Beniamini, P. & Kumar, P. 2016, MNRAS, 457, L108
- Beniamini, P. & Mochkovitch, R. 2017, A&A, 605, A60
- Bernardini, M. G., Margutti, R., Chincarini, G., Guidorzi, C., & Mao, J. 2011, A&A, 526, A27
- Bertin, E. 2006, in Astronomical Society of the Pacific Conference Series, Vol. 351, Astronomical Data Analysis Software and Systems XV, ed. C. Gabriel, C. Arviset, D. Ponz, & S. Enrique, 112
- Bertin, E. 2010, SWarp: Resampling and Co-adding FITS Images Together
- Bertin, E. & Arnouts, S. 1996, A&AS, 117, 393
- Bertin, E., Mellier, Y., Radovich, M., et al. 2002, in Astronomical Society of the Pacific Conference Series, Vol. 281, Astronomical Data Analysis Software and Systems XI, ed. D. A. Bohlender, D. Durand, & T. H. Handley, 228
- Bloom, J. S., Frail, D. A., & Kulkarni, S. R. 2003, ApJ, 594, 674
- Bochenek, A. & Perley, D. A. 2024a, GRB Coordinates Network, 37869, 1
- Bochenek, A. & Perley, D. A. 2024b, GRB Coordinates Network, 38030, 1
- Bradley, L., Sińczak, B., Robitaille, T., et al. 2024, astropy/photutils: 2.0.2
- Bright, J. S., Carotenuto, F., Fender, R., et al. 2024, arXiv e-prints, arXiv:2409.19055
- Burrows, D. N., Hill, J. E., Nousek, J. A., et al. 2005a, Space Sci. Rev., 120, 165
- Burrows, D. N., Romano, P., Falcone, A., et al. 2005b, Science, 309, 1833
- Cano, Z., Bersier, D., Guidorzi, C., et al. 2011, ApJ, 740, 41

- Cano, Z., Wang, S.-Q., Dai, Z.-G., & Wu, X.-F. 2017, *Advances in Astronomy*, 2017, 8292054
- Cappellaro, E., Mazzali, P. A., Benetti, S., et al. 1997, *A&A*, 328, 203
- Cenko, S. B., Kulkarni, S. R., Horesh, A., et al. 2013, *ApJ*, 769, 130
- Chambers, K. C., Magnier, E. A., Metcalfe, N., et al. 2016, arXiv e-prints, arXiv:1612.05560
- Chatzopoulos, E., Wheeler, J. C., Vinko, J., Horvath, Z. L., & Nagy, A. 2013, *ApJ*, 773, 76
- Chen, Z. H., Yan, L., Kangas, T., et al. 2023, *ApJ*, 943, 42
- Chevalier, R. A. & Li, Z.-Y. 2000, *ApJ*, 536, 195
- Chonis, T. S., Hill, G. J., Lee, H., Tuttle, S. E., & Vattiat, B. L. 2014, in *Society of Photo-Optical Instrumentation Engineers (SPIE) Conference Series*, Vol. 9147, *Ground-based and Airborne Instrumentation for Astronomy V*, ed. S. K. Ramsay, I. S. McLean, & H. Takami, 91470A
- Chonis, T. S., Hill, G. J., Lee, H., et al. 2016, in *Society of Photo-Optical Instrumentation Engineers (SPIE) Conference Series*, Vol. 9908, *Ground-based and Airborne Instrumentation for Astronomy VI*, ed. C. J. Evans, L. Simard, & H. Takami, 99084C
- Clark, P., Maguire, K., Inserra, C., et al. 2020, *MNRAS*, 492, 2208
- Coppejans, D. L., Margutti, R., Guidorzi, C., et al. 2018, *ApJ*, 856, 56
- Coppejans, D. L., Margutti, R., Terreran, G., et al. 2020, *ApJ*, 895, L23
- Covino, S., D'Avanzo, P., Klotz, A., et al. 2008, *MNRAS*, 388, 347
- Curran, P. A., Starling, R. L. C., O'Brien, P. T., et al. 2008, *A&A*, 487, 533
- Dai, Z. G. & Lu, T. 2002, *ApJ*, 565, L87
- Dainotti, M. G., Cardone, V. F., & Capozziello, S. 2008, *MNRAS*, 391, L79
- Dainotti, M. G., De Simone, B., Malik, R. F. M., et al. 2024, *MNRAS*[arXiv:2405.02263]
- Dalal, N., Griest, K., & Pruet, J. 2002, *ApJ*, 564, 209
- Das, K. K., Fremling, C., Kasliwal, M. M., et al. 2024, *ApJ*, 969, L11
- D'Elia, V., Campana, S., D'Ai, A., et al. 2018, *A&A*, 619, A66
- Dichiara, S., Troja, E., Lipunov, V., et al. 2022, *MNRAS*, 512, 2337
- Drout, M. R., Chornock, R., Soderberg, A. M., et al. 2014, *ApJ*, 794, 23
- Duque, R., Beniamini, P., Daigne, F., & Mochkovitch, R. 2022, *MNRAS*, 513, 951
- Eftekhari, T., Berger, E., Margalit, B., et al. 2019, *ApJ*, 876, L10
- Foreman-Mackey, D., Hogg, D. W., Lang, D., & Goodman, J. 2013, *PASP*, 125, 306
- Frail, D. A., Kulkarni, S. R., Sari, R., et al. 2001, *ApJ*, 562, L55
- Freeburn, J., Andreoni, I., & Carney, J. 2024a, *GRB Coordinates Network*, 37942, 1
- Freeburn, J., Cooke, J., Möller, A., et al. 2024b, arXiv e-prints, arXiv:2405.11949
- Fu, S. Y., Tinyanton, S., Anutarawiramkul, R., et al. 2024a, *GRB Coordinates Network*, 37842, 1
- Fu, S. Y., Zhu, Z. P., An, J., et al. 2024b, *GRB Coordinates Network*, 37840, 1
- Galama, T. J., Vreeswijk, P. M., van Paradijs, J., et al. 1998, *Nature*, 395, 670
- Galama, T. J., Vreeswijk, P. M., van Paradijs, J., et al. 1999, *A&AS*, 138, 465
- Gehrels, N., Chincarini, G., Giommi, P., et al. 2004, *ApJ*, 611, 1005
- Ghirlanda, G., Ghisellini, G., Nava, L., et al. 2012, *MNRAS*, 422, 2553
- Ghirlanda, G., Nappo, F., Ghisellini, G., et al. 2018, *A&A*, 609, A112
- Ghirlanda, G., Salafia, G. S., Paragi, Z., et al. 2019, *Science*, 363, 968
- Ghisellini, G., Ghirlanda, G., Nava, L., & Celotti, A. 2010, *MNRAS*, 403, 926
- Gill, R. & Granot, J. 2023, *MNRAS*, 524, L78
- Gillanders, J. H., Rhodes, L., Srivastav, S., et al. 2024, *ApJ*, 969, L14
- Gomez, S., Berger, E., Nicholl, M., Blanchard, P. K., & Hosseinzadeh, G. 2022, *ApJ*, 941, 107
- Gomez, S., Nicholl, M., Berger, E., et al. 2024, *MNRAS*, 535, 471
- Goodman, J. 1986, *ApJ*, 308, L47
- Gössl, C. A. & Riffeser, A. 2002, *A&A*, 381, 1095
- Granot, J., Nakar, E., & Piran, T. 2003, *Nature*, 426, 138
- Granot, J. & Sari, R. 2002, *ApJ*, 568, 820
- Guillochon, J., Nicholl, M., Villar, V. A., et al. 2018, *ApJS*, 236, 6
- H. E. S. S. Collaboration, Abdalla, H., Aharonian, F., et al. 2021, *Science*, 372, 1081
- Hill, G. J., Lee, H., MacQueen, P. J., et al. 2021, *AJ*, 162, 298
- Hinton, S. R. 2016, *The Journal of Open Source Software*, 1, 00045
- Hjorth, J. & Bloom, J. S. 2012, in *Chapter 9 in "Gamma-Ray Bursts*, ed. C. Kouveliotou, R. A. M. J. Wijers, & S. Woosley, 169–190
- Ho, A. Y. Q., Perley, D. A., Chen, P., et al. 2023a, *Nature*, 623, 927
- Ho, A. Y. Q., Perley, D. A., Gal-Yam, A., et al. 2023b, *ApJ*, 949, 120
- Ho, A. Y. Q., Perley, D. A., Kulkarni, S. R., et al. 2020, *ApJ*, 895, 49
- Ho, A. Y. Q., Perley, D. A., Yao, Y., et al. 2022, *ApJ*, 938, 85
- Ho, A. Y. Q., Phinney, E. S., Ravi, V., et al. 2019, *ApJ*, 871, 73
- Hopp, U., Bender, R., Grupp, F., et al. 2014, in *Society of Photo-Optical Instrumentation Engineers (SPIE) Conference Series*, Vol. 9145, *Ground-based and Airborne Telescopes V*, ed. L. M. Stepp, R. Gilmozzi, & H. J. Hall, 91452D
- Hu, J. W., Wang, Y., He, H., et al. 2024, *GRB Coordinates Network*, 37834, 1
- Huang, Y. F., Dai, Z. G., & Lu, T. 2002, *MNRAS*, 332, 735
- Irwin, C. M. & Hotokezaka, K. 2024a, arXiv e-prints, arXiv:2412.06733
- Irwin, C. M. & Hotokezaka, K. 2024b, arXiv e-prints, arXiv:2412.06734
- Irwin, C. M. & Hotokezaka, K. 2024c, arXiv e-prints, arXiv:2412.06736
- Iwamoto, K., Mazzali, P. A., Nomoto, K., et al. 1998, *Nature*, 395, 672
- Izzo, L., de Ugarte Postigo, A., Maeda, K., et al. 2019, *Nature*, 565, 324
- Jiang, S.-Q., Xu, D., van Hoof, A. P. C., et al. 2025, arXiv e-prints, arXiv:2503.04306
- Jóhannesson, G., Björnsson, G., & Gudmundsson, E. H. 2006, *ApJ*, 647, 1238
- Kissler-Patig, M., Pirard, J. F., Casali, M., et al. 2008, *A&A*, 491, 941
- Klingler, N., Oates, S. R., Eyles-Ferris, R., & Swift-UVOT Team. 2024, *GRB Coordinates Network*, 37990, 1
- Knust, F., Greiner, J., van Eerten, H. J., et al. 2017, *A&A*, 607, A84
- Koposov, S., Speagle, J., Barbary, K., et al. 2024, *joshspeagle/dynesty: v2.1.4*
- Kumar, H., Gupta, R., Saraogi, D., et al. 2022, *MNRAS*, 513, 2777
- Kumar, P. & Panaitescu, A. 2000, *ApJ*, 541, L51
- Lamb, G. P., Tanvir, N. R., Levan, A. J., et al. 2019, *ApJ*, 883, 48
- Lamberts, A. & Daigne, F. 2018, *MNRAS*, 474, 2813
- Lang-Bardl, F., Bender, R., Goessl, C., et al. 2016, in *Society of Photo-Optical Instrumentation Engineers (SPIE) Conference Series*, Vol. 9908, *Ground-based and Airborne Instrumentation for Astronomy VI*, ed. C. J. Evans, L. Simard, & H. Takami, 990844
- Laskar, T., Alexander, K. D., Margutti, R., et al. 2023, *ApJ*, 946, L23
- Law, C. J., Gaensler, B. M., Metzger, B. D., Ofek, E. O., & Sironi, L. 2018, *ApJ*, 866, L22
- Levan, A. J., Jonker, P. G., Saccardi, A., et al. 2024, arXiv e-prints, arXiv:2404.16350
- Levinson, A., Ofek, E. O., Waxman, E., & Gal-Yam, A. 2002, *ApJ*, 576, 923
- Li, M. L., Ho, A. Y. Q., Ryan, G., et al. 2024a, arXiv e-prints, arXiv:2411.07973
- Li, W. X., Sun, N. C., Maund, J., Wang, Y. N., & Wiersema, K. 2024b, *GRB Coordinates Network*, 37846, 1
- Li, W. X., Xue, S. J., Andrews, M., et al. 2024c, *GRB Coordinates Network*, 37844, 1
- Lien, A., Sakamoto, T., Barthelmy, S. D., et al. 2016, *ApJ*, 829, 7
- Lipunov, V., Kornilov, V., Zhirkov, K., et al. 2022, *MNRAS*, 516, 4980
- Liu, Y., Sun, H., Xu, D., et al. 2024, arXiv e-prints, arXiv:2404.16425
- Malesani, D., Tagliaferri, G., Chincarini, G., et al. 2004, *ApJ*, 609, L5
- Margutti, R., Bernardini, G., Barniol Duran, R., et al. 2011, *MNRAS*, 410, 1064
- Margutti, R., Metzger, B. D., Chornock, R., et al. 2019, *ApJ*, 872, 18
- Meegan, C., Lichti, G., Bhat, P. N., et al. 2009, *ApJ*, 702, 791
- Melandri, A., Virgili, F. J., Guidorzi, C., et al. 2014, *A&A*, 572, A55
- Molinari, E., Vergani, S. D., Malesani, D., et al. 2007, *A&A*, 469, L13
- Mooley, K. P., Deller, A. T., Gottlieb, O., et al. 2018, *Nature*, 561, 355
- Mooley, K. P., Margalit, B., Law, C. J., et al. 2022, *ApJ*, 924, 16
- Moore, T., Gillanders, J. H., Nicholl, M., et al. 2024, arXiv e-prints, arXiv:2405.13596
- Moss, M. J., Mochkovitch, R., Daigne, F., Beniamini, P., & Guiriec, S. 2023, *MNRAS*, 525, 5224
- Nadyozhin, D. K. 1994, *ApJS*, 92, 527
- Nakar, E. & Granot, J. 2007, *MNRAS*, 380, 1744
- Nakar, E., Piran, T., & Granot, J. 2002, *ApJ*, 579, 699
- Nakar, E., Piran, T., & Granot, J. 2003, *New A*, 8, 495
- Nappo, F., Ghisellini, G., Ghirlanda, G., et al. 2014, *MNRAS*, 445, 1625
- Nava, L., Sironi, L., Ghisellini, G., Celotti, A., & Ghirlanda, G. 2013, *MNRAS*, 433, 2107
- Nicholl, M., Blanchard, P. K., Berger, E., et al. 2020, *Nature Astronomy*, 4, 893
- Nicholl, M., Guillochon, J., & Berger, E. 2017, *ApJ*, 850, 55
- O'Connor, B., Beniamini, P., & Gill, R. 2024, *MNRAS*[arXiv:2406.05297]
- O'Connor, B., Beniamini, P., & Kouveliotou, C. 2020, *MNRAS*, 495, 4782
- O'Connor, B., Pasham, D., Andreoni, I., et al. 2025, *ApJ*, 979, L30
- O'Connor, B., Troja, E., Ryan, G., et al. 2023, *Science Advances*, 9, eadi1405
- Ofek, E. O., Cenko, S. B., Gal-Yam, A., et al. 2007, *ApJ*, 662, 1129
- Panaitescu, A. 2008, *MNRAS*, 383, 1143
- Panaitescu, A. & Vestrand, W. T. 2011, *MNRAS*, 414, 3537
- Pérez-Fouron, I., Sun, N. C., Li, W., et al. 2024, *GRB Coordinates Network*, 37858, 1
- Perley, D. A., Ho, A. Y. Q., Fausnaugh, M., et al. 2024, arXiv e-prints, arXiv:2401.16470
- Perley, D. A., Ho, A. Y. Q., Yao, Y., et al. 2021, *MNRAS*, 508, 5138
- Perley, D. A., Mazzali, P. A., Yan, L., et al. 2019, *MNRAS*, 484, 1031
- Planck Collaboration, Aghanim, N., Akrami, Y., et al. 2020, *A&A*, 641, A6
- Prentice, S. J., Maguire, K., Smartt, S. J., et al. 2018, *ApJ*, 865, L3
- Pugliese, G., Xu, D., Izzo, L., et al. 2024, *GRB Coordinates Network*, 37852, 1
- Pursiainen, M., Childress, M., Smith, M., et al. 2018, *MNRAS*, 481, 894
- Quirola-Vásquez, J., Bauer, F. E., Jonker, P. G., et al. 2024, *A&A*, 683, A243
- Quirola-Vásquez, J., Bauer, F. E., Jonker, P. G., et al. 2023, *A&A*, 675, A44
- Quirola-Vásquez, J., Bauer, F. E., Jonker, P. G., et al. 2022, *A&A*, 663, A168
- Quirola-Vásquez, J. A., Malesani, D. B., Levan, A. J., Bauer, F. E., & Jonker, P. G. 2024, *GRB Coordinates Network*, 37930, 1
- Ramirez-Ruiz, E., Dray, L. M., Madau, P., & Tout, C. A. 2001, *MNRAS*, 327, 829

- Ramsey, L. W., Adams, M. T., Barnes, T. G., et al. 1998, in Society of Photo-Optical Instrumentation Engineers (SPIE) Conference Series, Vol. 3352, Advanced Technology Optical/IR Telescopes VI, ed. L. M. Stepp, 34–42
- Rees, M. J. & Mészáros, P. 1998, *ApJ*, 496, L1
- Reichherzer, P., Schüssler, F., Lefranc, V., et al. 2021, *ApJS*, 256, 5
- Rhoads, J. E. 1999, *ApJ*, 525, 737
- Rhoads, J. E. 2003, *ApJ*, 591, 1097
- Ricci, R., Bruni, G., Carotenuto, F., Gianfagna, G., & Yao, Y. 2024a, GRB Coordinates Network, 37949, 1
- Ricci, R., Troja, E., Yang, Y., et al. 2024b, arXiv e-prints, arXiv:2407.18311
- Roming, P. W. A., Kennedy, T. E., Mason, K. O., et al. 2005, *Space Sci. Rev.*, 120, 95
- Ror, A. K., Gupta, A., Tripathi, T., Pandey, S. B., & Mishra, K. 2024, GRB Coordinates Network, 37845, 1
- Rouco Escorial, A., Fong, W.-f., Berger, E., et al. 2022, arXiv e-prints, arXiv:2210.05695
- Ryan, G., van Eerten, H., Troja, E., et al. 2023, arXiv e-prints, arXiv:2310.02328
- Sakamoto, T., Barthelmy, S. D., Baumgartner, W. H., et al. 2011, *ApJS*, 195, 2
- Sakamoto, T., Lamb, D. Q., Graziani, C., et al. 2004, *ApJ*, 602, 875
- Sari, R. & Mészáros, P. 2000, *ApJ*, 535, L33
- Sari, R. & Piran, T. 1995, *ApJ*, 455, L143
- Sari, R. & Piran, T. 1999, *ApJ*, 520, 641
- Sari, R., Piran, T., & Halpern, J. P. 1999, *ApJ*, 519, L17
- Schlaflly, E. F. & Finkbeiner, D. P. 2011, *ApJ*, 737, 103
- Schneider, B. & Adami, C. 2024a, GRB Coordinates Network, 38071, 1
- Schneider, B. & Adami, C. 2024b, GRB Coordinates Network, 38022, 1
- Schroeder, G., Srinivasaragavan, G., Ho, A., et al. 2024, GRB Coordinates Network, 38640, 1
- Shetrone, M., Cornell, M. E., Fowler, J. R., et al. 2007, *PASP*, 119, 556
- Skrutskie, M. F., Cutri, R. M., Stiening, R., et al. 2006, *AJ*, 131, 1163
- Soderberg, A. M., Kulkarni, S. R., Berger, E., et al. 2004a, *ApJ*, 606, 994
- Soderberg, A. M., Kulkarni, S. R., Berger, E., et al. 2004b, *Nature*, 430, 648
- Soderberg, A. M., Kulkarni, S. R., Nakar, E., et al. 2006, *Nature*, 442, 1014
- Soderberg, A. M., Nakar, E., Cenko, S. B., et al. 2007, *ApJ*, 661, 982
- Speagle, J. S. 2020, *MNRAS*, 493, 3132
- Srinivasaragavan, G. P., Perley, D. A., Ho, A. Y. Q., et al. 2025, *MNRAS*[arXiv:2501.03337]
- Srivastav, S., Chen, T. W., Gillanders, J. H., et al. 2024, arXiv e-prints, arXiv:2409.19070
- Starling, R. L. C., Wiersema, K., Levan, A. J., et al. 2011, *MNRAS*, 411, 2792
- Sun, H., Li, W. X., Liu, L. D., et al. 2024, arXiv e-prints, arXiv:2410.02315
- Suzuki, A., Nicholl, M., Moriya, T. J., & Takiwaki, T. 2021, *ApJ*, 908, 99
- Svinkin, D., Frederiks, D., & Konus-Wind team. 2024, GRB Coordinates Network, 38034, 1
- Swenson, C. A., Roming, P. W. A., De Pasquale, M., & Oates, S. R. 2013, *ApJ*, 774, 2
- Tang, C.-H., Huang, Y.-F., Geng, J.-J., & Zhang, Z.-B. 2019, *ApJS*, 245, 1
- Thompson, C. 1994, *MNRAS*, 270, 480
- Totani, T. & Panaitescu, A. 2002, *ApJ*, 576, 120
- Troja, E., Cusumano, G., O’Brien, P. T., et al. 2007, *ApJ*, 665, 599
- van Dalen, J. N. D., Levan, A. J., Jonker, P. G., et al. 2024, arXiv e-prints, arXiv:2409.19056
- van Eerten, H. J., Meliani, Z., Wijers, R. A. M. J., & Keppens, R. 2009, *MNRAS*, 398, L63
- Villar, V. A., Berger, E., Metzger, B. D., & Guillochon, J. 2017, *ApJ*, 849, 70
- Vinkó, J., Yuan, F., Quimby, R. M., et al. 2015, *ApJ*, 798, 12
- Wang, X.-G., Zhang, B., Liang, E.-W., et al. 2018, *ApJ*, 859, 160
- Willingale, R., Starling, R. L. C., Beardmore, A. P., Tanvir, N. R., & O’Brien, P. T. 2013, *MNRAS*, 431, 394
- Xu, F., Tang, C.-H., Geng, J.-J., et al. 2021, *ApJ*, 920, 135
- Yao, Y., De, K., Kasliwal, M. M., et al. 2020, *ApJ*, 900, 46
- Yin, Y.-H. I., Zhang, B.-B., Yang, J., et al. 2024, arXiv e-prints, arXiv:2407.10156
- Yuan, W., Dai, L., Feng, H., et al. 2025, arXiv e-prints, arXiv:2501.07362
- Yuan, W., Zhang, C., Chen, Y., & Ling, Z. 2022, in *Handbook of X-ray and Gamma-ray Astrophysics*, 86
- Yuan, W., Zhang, C., Feng, H., et al. 2015, arXiv e-prints, arXiv:1506.07735
- Zhang, B., Fan, Y. Z., Dyks, J., et al. 2006, *ApJ*, 642, 354
- Zhang, B., Wang, X.-Y., & Zheng, J.-H. 2024, *Journal of High Energy Astrophysics*, 41, 42
- Zhang, W., Yuan, W., Ling, Z., et al. 2025, *Science China Physics, Mechanics, and Astronomy*, 68, 219511
- Zheng, W., Brink, T. G., Filippenko, A. V., Yang, Y., & KAIT GRB Team. 2024a, GRB Coordinates Network, 38294, 1
- Zheng, W., Han, X., Zhang, P., Filippenko, V. A., & KAIT GRB team. 2024b, GRB Coordinates Network, 37849, 1

Appendix A: Log of Observations

Here we report the list of observations of EP241021a analyzed as part of this work. The observations are tabulated in Table A.1 and A.2.

Table A.1: Log of optical and near-infrared imaging observations used in this work. The photometry is not corrected for Galactic extinction $E(B - V) = 0.045$ mag (Schlafly & Finkbeiner 2011). The Galactic extinction in a given bandpass is tabulated below as A_λ (Schlafly & Finkbeiner 2011).

Start Time (UT)	δT (d)	Telescope	Instrument	Exposure (s)	Filter	AB magnitude	A_λ (mag)
Wendelstein Observatory							
2024-10-24T02:12:17	2.88	FTW	3KK	1980	<i>r</i>	22.48± 0.16	0.10
2024-10-24T02:12:17	2.88	FTW	3KK	1980	<i>z</i>	21.55± 0.21	0.06
2024-10-24T02:12:31	2.88	FTW	3KK	1867	<i>J</i>	21.04± 0.21	0.04
2024-10-24T23:42:00	3.77	FTW	3KK	7200	<i>r</i>	22.47± 0.10	0.10
2024-10-24T23:42:00	3.77	FTW	3KK	7200	<i>z</i>	22.20± 0.12	0.06
2024-10-24T23:42:14	3.77	FTW	3KK	6790	<i>J</i>	21.73± 0.12	0.04
2024-10-25T21:27:05	4.68	FTW	3KK	9540	<i>r</i>	22.69± 0.10	0.10
2024-10-25T21:27:05	4.68	FTW	3KK	9540	<i>z</i>	22.50± 0.21	0.06
2024-10-25T21:27:20	4.68	FTW	3KK	8147	<i>J</i>	22.08± 0.23	0.04
2024-10-26T19:25:35	5.60	FTW	3KK	5580	<i>r</i>	22.93± 0.18	0.10
2024-10-26T19:25:35	5.60	FTW	3KK	5400	<i>z</i>	>22.2	0.06
2024-10-26T19:25:49	5.60	FTW	3KK	5262	<i>J</i>	21.44± 0.26	0.04
2024-10-28T21:04:27	7.66	FTW	3KK	5580	<i>r</i>	21.67± 0.10	0.10
2024-10-28T21:04:27	7.66	FTW	3KK	5580	<i>z</i>	21.20± 0.10	0.06
2024-10-28T21:08:46	7.67	FTW	3KK	5092	<i>J</i>	20.79± 0.10	0.04
2024-10-29T19:23:45	8.59	FTW	3KK	4500	<i>r</i>	21.63± 0.10	0.10
2024-10-29T19:23:45	8.59	FTW	3KK	4500	<i>z</i>	21.09± 0.10	0.06
2024-10-29T19:23:59	8.59	FTW	3KK	3904	<i>J</i>	20.77± 0.10	0.04
2024-10-31T00:20:10	9.80	FTW	3KK	5040	<i>r</i>	21.32± 0.10	0.10
2024-10-31T00:20:10	9.80	FTW	3KK	5040	<i>z</i>	21.80± 0.10	0.06
2024-10-31T00:20:24	9.80	FTW	3KK	4753	<i>J</i>	20.92± 0.10	0.04
2024-10-31T18:40:04	10.56	FTW	3KK	7200	<i>r</i>	21.87± 0.10	0.10
2024-10-31T18:40:04	10.56	FTW	3KK	7200	<i>z</i>	21.47± 0.10	0.06
2024-10-31T18:40:18	10.56	FTW	3KK	6450	<i>J</i>	21.12± 0.10	0.04
2024-11-01T22:17:50	11.72	FTW	3KK	7200	<i>r</i>	22.23± 0.10	0.10
2024-11-01T22:17:50	11.72	FTW	3KK	7020	<i>z</i>	21.66± 0.10	0.06
2024-11-01T22:18:04	11.72	FTW	3KK	6790	<i>J</i>	21.24± 0.10	0.04
2024-11-03T19:34:27	13.60	FTW	3KK	7200	<i>r</i>	22.30± 0.10	0.10
2024-11-03T19:34:27	13.60	FTW	3KK	7200	<i>z</i>	21.84± 0.12	0.06
2024-11-03T19:34:41	13.60	FTW	3KK	6790	<i>J</i>	21.90± 0.20	0.04
2024-11-04T23:53:42	14.78	FTW	3KK	6480	<i>r</i>	22.61± 0.10	0.10
2024-11-04T23:53:42	14.78	FTW	3KK	6480	<i>z</i>	21.80± 0.10	0.06
2024-11-04T23:53:56	14.78	FTW	3KK	6111	<i>J</i>	21.78± 0.14	0.04
2024-11-06T01:11:18	15.84	FTW	3KK	3780	<i>r</i>	22.73± 0.10	0.10
2024-11-06T01:11:18	15.84	FTW	3KK	3780	<i>z</i>	22.00± 0.14	0.06
2024-11-06T01:11:32	15.84	FTW	3KK	3395	<i>J</i>	21.87± 0.20	0.04
2024-11-07T21:53:13	17.70	FTW	3KK	7200	<i>r</i>	22.80± 0.10	0.10
2024-11-07T21:53:13	17.70	FTW	3KK	7200	<i>z</i>	21.97± 0.11	0.06
2024-11-07T21:53:27	17.70	FTW	3KK	6790	<i>J</i>	21.93± 0.16	0.04
2024-11-08T22:55:09	18.74	FTW	3KK	4860	<i>r</i>	23.2 ± 0.3	0.10
2024-11-08T22:55:09	18.74	FTW	3KK	4680	<i>z</i>	>22.1	0.06
2024-11-08T23:02:27	18.75	FTW	3KK	1188	<i>J</i>	>21.2	0.04
2024-11-10T22:29:33	20.72	FTW	3KK	1800	<i>r</i>	22.59± 0.11	0.10
2024-11-10T22:29:33	20.72	FTW	3KK	1800	<i>z</i>	22.26± 0.22	0.06
2024-11-10T22:29:47	20.72	FTW	3KK	1528	<i>J</i>	>22.3	0.04
2024-11-12T19:22:13	22.59	FTW	3KK	5400	<i>r</i>	22.64± 0.12	0.10
2024-11-12T19:22:13	22.59	FTW	3KK	5400	<i>z</i>	22.15± 0.16	0.06
2024-11-12T19:22:28	22.59	FTW	3KK	5092	<i>J</i>	22.28± 0.22	0.04
2024-11-16T18:12:12	26.54	FTW	3KK	4140	<i>r</i>	23.3 ± 0.4	0.10
2024-11-16T18:12:12	26.54	FTW	3KK	3960	<i>z</i>	22.7 ± 0.4	0.06
2024-11-16T18:12:26	26.54	FTW	3KK	3904	<i>J</i>	>22.5	0.04

Continued on next page

Table A.1: (continued)

Start Time (UT)	δT (d)	Telescope	Instrument	Exposure (s)	Filter	AB magnitude	A_{λ} (mag)
2024-11-24T20:59:23	34.66	FTW	3KK	9180	<i>r</i>	>23.3	0.10
2024-11-24T20:59:23	34.66	FTW	3KK	9360	<i>z</i>	>22.1	0.06
2024-11-24T20:59:37	34.66	FTW	3KK	8703	<i>J</i>	>21.7	0.04
2024-11-25T21:53:13	35.70	FTW	3KK	3600	<i>r</i>	>23.5	0.10
2024-11-25T21:53:13	35.70	FTW	3KK	3600	<i>z</i>	>21.9	0.06
2024-11-25T21:53:27	35.70	FTW	3KK	3395	<i>J</i>	>21.3	0.04
2024-11-27T19:31:59	37.60	FTW	3KK	4320	<i>r</i>	23.39± 0.23	0.10
2024-11-27T19:31:59	37.60	FTW	3KK	3420	<i>z</i>	>22.5	0.06
2024-11-27T19:32:13	37.60	FTW	3KK	3565	<i>J</i>	>21.9	0.04
2024-11-30T18:51:08	40.57	FTW	3KK	14 220	<i>r</i>	24.06± 0.19	0.10
2024-11-30T18:51:08	40.57	FTW	3KK	14 400	<i>z</i>	>23.3	0.06
2024-11-30T18:51:22	40.57	FTW	3KK	13 579	<i>J</i>	22.46± 0.23	0.04
2024-12-01T18:26:24	41.55	FTW	3KK	10 850	<i>r</i>	23.49± 0.12	0.10
2024-12-01T18:26:24	41.55	FTW	3KK	10 850	<i>i</i>	23.35± 0.15	0.08
2024-12-01T18:26:38	41.55	FTW	3KK	9145	<i>H</i>	>22.3	0.02
Very Large Telescope							
2024-12-05T01:48:40	45.2	VLT	FORS2	1200	<i>R</i>	23.9 ± 0.1	0.12
2024-12-05T02:13:04	45.2	VLT	HAWK-I	900	<i>J</i>	23.0 ± 0.1	0.04
2024-12-22T01:02:41	61.8	VLT	HAWK-I	900	<i>J</i>	23.3 ± 0.1	0.04
2024-12-28T02:12:42	67.9	VLT	FORS2	1200	<i>R</i>	24.90± 0.15	0.12
2025-01-23T01:04:23	93.8	VLT	HAWK-I	1200	<i>J</i>	24.02± 0.15	0.04
2025-01-23T01:32:49	93.8	VLT	FORS2	1200	<i>R</i>	24.8 ± 0.1	0.12
Swift/UVOT							
2024-10-24T20:58:13	3.66	<i>Swift</i>	UVOT	2545	<i>v</i>	>20.5	0.14
2024-10-24T21:08:18	3.67	<i>Swift</i>	UVOT	163	<i>b</i>	>19.8	0.17
2024-10-25T15:30:30	4.43	<i>Swift</i>	UVOT	1347	<i>uvm2</i>	>22.4	0.39
2024-10-29T09:32:49	8.18	<i>Swift</i>	UVOT	4289	<i>u</i>	21.85± 0.23	0.22
2024-11-03T02:25:38	12.88	<i>Swift</i>	UVOT	3059	<i>u</i>	>22.3	0.22
2024-11-05T20:24:14	15.63	<i>Swift</i>	UVOT	985	<i>u</i>	>21.7	0.22
2024-11-07T02:15:17	16.88	<i>Swift</i>	UVOT	3107	<i>u</i>	>22.3	0.22
2024-11-15T19:08:48	25.58	<i>Swift</i>	UVOT	1676	<i>u</i>	>22.0	0.22

Table A.2: Log of optical spectroscopic observations used in this work.

Start Time (UT)	δT (d)	Telescope	Instrument	Exposure (s)
2024-10-25T04:25	5.0	HET	LRS-B	3000
2024-10-29T07:43	9.1	HET	LRS-R	2050
2024-11-26T05:43	37.0	HET	LRS-R	3600

Table A.3: Log of X-ray observations used in this work. The unabsorbed flux is given in the 0.3 – 10 keV band and flux density F_{ν} at 1 keV.

Start Time (UT)	δT (d)	Telescope	Instrument	Exposure (s)	Flux ($\text{erg cm}^{-2} \text{s}^{-1}$)
2024-10-24T20:54:12	3.66	<i>Swift</i>	XRT	2770	$< 2.5 \times 10^{-13}$
2024-10-25T15:26:02	4.43	<i>Swift</i>	XRT	1380	$< 3.9 \times 10^{-13}$
2024-10-29T09:30:13	8.18	<i>Swift</i>	XRT	4385	$(1.4^{+0.6}_{-0.5}) \times 10^{-13}$
2024-11-03T02:22:02	12.88	<i>Swift</i>	XRT	3120	$< 1.8 \times 10^{-13}$
2024-11-05T20:21:02	15.63	<i>Swift</i>	XRT	1005	$< 5.6 \times 10^{-13}$
2024-11-07T02:13:02	16.88	<i>Swift</i>	XRT	3180	$(5.5^{+0.3}_{-0.3}) \times 10^{-14}$
2024-11-15T19:06:02	25.58	<i>Swift</i>	XRT	1710	$(7.9^{+0.6}_{-0.4}) \times 10^{-14}$

Appendix B: Corner Plot Results of OIR Lightcurve Fitting

Here we show the corner plot (Figure B.1) of the lightcurve fitting results, see also §3.1.

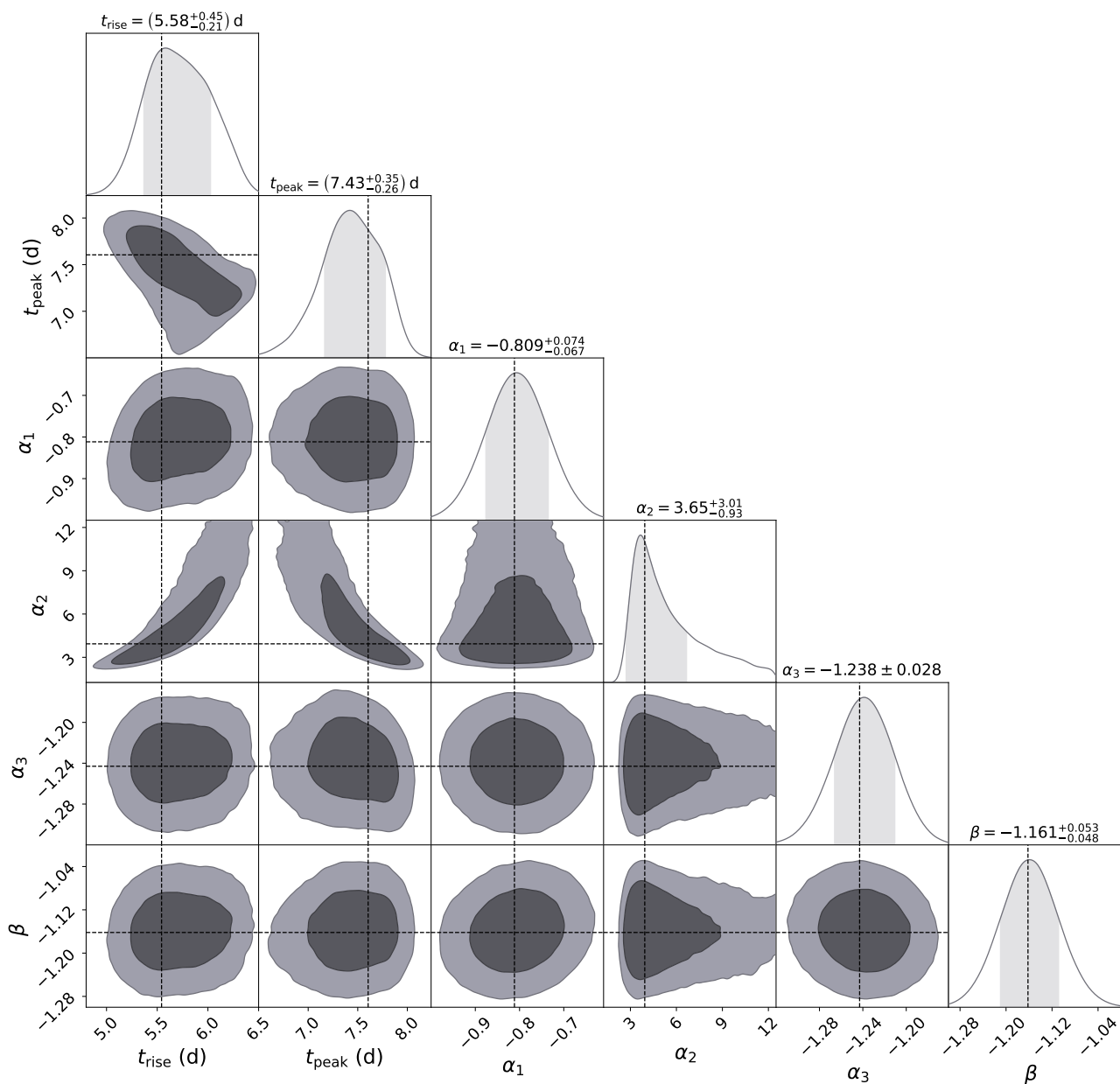


Fig. B.1: Corner plot for the temporal and spectral powerlaw fit $F_\nu \propto t^\alpha \nu^\beta$ to the multi-band *riJ* lightcurves of EP241021a (see §3.1). The dashed lines indicate the best fit values.

Appendix C: Supernova Model Fitting

In Table C.1, we display the priors used in our MOSFiT modeling (see also §4.7.1). In Table C.2, the posteriors from each model fitted by MOSFiT are displayed.

Table C.1: Model Parameters (Footnotes: a: κ_γ was not specified in csm; b: to get this range of E_{kin} , we set $M_{\text{ej}} \in [0.1, 200] M_\odot$ and $v_{\text{ej}} \in \log([10^3, 10^5]) \text{ km s}^{-1}$; c: κ was not specified in csm; d: the magnetar model does not use f_{Ni} ; e: the csm model does not use f_{Ni} ; f: v_{ej} in csmni is already embedded in E_{kin}).

Prior	default	magni	csmni
$\kappa_\gamma [\text{cm}^2 \text{g}^{-1}]$	2.70×10^{-2}	2.70×10^{-2}	2.70×10^{-2a}
$E_{\text{kin}} [10^{51} \text{erg}]$	–	–	$\log([10^{-1}, 10^2])^b$
s	–	–	[0.00, 2.00]
$\rho [\text{g cm}^3]$	–	–	$\log([10^{-15}, 10^{-11}])$
$T [\text{K}]$	$\log([3.00 \times 10^3, 10^4])$	$\log([3.00 \times 10^3, 10^4])$	$\log([10^3, 10^5])$
$M_{\text{ej}} [M_\odot]$	$[10^{-1}, 10^2]$	$[10^{-1}, 10^2]$	$[10^{-1}, 2.00 \times 10^2]$
$\kappa [\text{cm}^2 \text{g}^{-1}]$	$[5.00 \times 10^{-2}, 3.40 \times 10^{-1}]$	$[5.00 \times 10^{-2}, 3.40 \times 10^{-1}]$	$[5.00 \times 10^{-2}, 3.40 \times 10^{-1}]^c$
σ	$\log([10^{-3}, 10^2])$	$\log([10^{-3}, 10^2])$	$\log([10^{-5}, 10^1])$
$M_{\text{CSM}} [M_\odot]$	–	–	$[10^{-1}, 2.00 \times 10^2]$
f_{Ni}	$[10^{-2}, 5.00 \times 10^{-1}]$	$[10^{-2}, 5.00 \times 10^{-1}]^d$	$[10^{-2}, 5.00 \times 10^{-1}]^e$
$r_0 [\text{AU}]$	–	–	$\log([10^{-2}, 10^2])$
$M_{\text{NS}} [M_\odot]$	–	[1.50, 1.90]	–
$v_{\text{ej}} [\text{km s}^{-1}]$	$[10^3, 10^5]$	$[10^3, 10^5]$	– ^f
$B_{\text{field}} [10^{14} \text{G}]$	–	$[10^{-1}, 1.50 \times 10^1]$	–
δ	–	–	0.00
$P_{\text{spin}} [\text{ms}]$	–	$[7.00 \times 10^{-1}, 10^1]$	–
$\theta_{\text{PB}} [\text{radians}]$	–	[0.00, 1.57]	–
n	–	–	$[7.00, 1.20 \times 10^1]$

Table C.2: Posteriors of the models default, magnetar, magni, csm, and csmni.

Parameter	default	magnetar	magni	csm	csmni
$P_{\text{spin}} [\text{ms}]$	–	$0.95^{+0.36}_{-0.19}$	$1.2^{+0.8}_{-0.4}$	–	–
$v_{\text{ej}} [\text{km s}^{-1}]$	97000^{+2200}_{-4400}	95800^{+3000}_{-5500}	96900^{+2300}_{-4700}	79400^{+5700}_{-5300}	–
$\log(E_{\text{kin}} [10^{51} \text{erg}])$	–	–	–	–	$1.96^{+0.03}_{-0.06}$
$\log(T [\text{K}])$	$3.88^{+0.05}_{-0.04}$	$3.78^{+0.05}_{-0.04}$	$3.85^{+0.04}_{-0.04}$	$4.82^{+0.04}_{-0.04}$	$4.13^{+0.03}_{-0.03}$
$M_{\text{NS}} [M_\odot]$	–	$1.76^{+0.10}_{-0.14}$	$1.70^{+0.13}_{-0.13}$	–	–
$M_{\text{ej}} [M_\odot]$	$9.9^{+1.0}_{-0.9}$	$36.8^{+14.7}_{-7.2}$	$12.4^{4.3}_{-2.1}$	118^{+54}_{-60}	$2.9^{+0.6}_{-0.5}$
$B_{\text{field}} [10^{14} \text{G}]$	–	$7.5^{+2.9}_{-1.7}$	$11.9^{+2.00}_{-2.2}$	–	–
$M_{\text{CSM}} [M_\odot]$	–	–	–	$2.1^{+0.4}_{-0.5}$	95^{+66}_{-65}
$\log(\rho [\text{g cm}^3])$	–	–	–	$-12.0^{+0.6}_{-0.8}$	$-12.8^{+1.0}_{-0.8}$
$r_0 [\text{AU}]$	–	–	–	$0.8^{+0.6}_{-0.4}$	$1.2^{+0.5}_{-0.5}$
f_{Ni}	$0.47^{+0.02}_{-0.03}$	–	$0.32^{+0.12}_{-0.14}$	–	$0.33^{+0.12}_{-0.17}$
$A_V [\text{mag}]$	$0.00^{0.01}_{-0.00}$	$0.00^{0.01}_{-0.00}$	$0.00^{0.01}_{-0.00}$	$2.49^{0.08}_{-0.08}$	$1.68^{0.11}_{-0.12}$